

Radiative and mechanical feedback into the molecular gas in the Large Magellanic Cloud

I. N159W^{★,★★}

M.-Y. Lee¹, S. C. Madden¹, V. Lebouteiller¹, A. Gusdorf^{2,3}, B. Godard⁴, R. Wu⁵, M. Galametz⁶, D. Cormier⁷,
F. Le Petit⁴, E. Roueff⁴, E. Bron^{4,8}, L. Carlson⁹, M. Chevance¹, Y. Fukui¹⁰, F. Galliano¹, S. Hony⁷, A. Hughes¹¹,
R. Indebetouw^{12,13}, F. P. Israel¹⁴, A. Kawamura¹⁵, J. Le Bourlot⁴, P. Lesaffre^{2,3}, M. Meixner¹⁶, E. Muller¹⁵,
O. Nayak¹⁷, T. Onishi¹⁸, J. Roman-Duval¹⁶, and M. Sewifo¹⁹

¹ Laboratoire AIM, CEA/IRFU/Service d'Astrophysique, Bât. 709, 91191 Gif-sur-Yvette, France
e-mail: min-young.lee@cea.fr

² LERMA, Observatoire de Paris, École Normale Supérieure, PSL Research University, CNRS, UMR 8112, 75014 Paris, France

³ Sorbonne Universités, UPMC Univ. Paris 6, UMR 8112, LERMA, 75005 Paris, France

⁴ LERMA, Observatoire de Paris, PSL Research University, CNRS, UMR 8112, 92190 Meudon, France

⁵ International Research Fellow of the Japan Society for the Promotion of Science (JSPS), Department of Astronomy,
University of Tokyo, Bunkyo-ku, 113-0033 Tokyo, Japan

⁶ European Southern Observatory, Karl-Schwarzschild-Str. 2, 85748 Garching-bei-München, Germany

⁷ Institut für Theoretische Astrophysik, Zentrum für Astronomie der Universität Heidelberg, Albert-Ueberle Str. 2,
69120 Heidelberg, Germany

⁸ ICMM, Consejo Superior de Investigaciones Científicas, 28049 Madrid, Spain

⁹ Harvard-Smithsonian Center for Astrophysics, 60 Garden St., Cambridge, MA 02138, USA

¹⁰ Department of Physics, Nagoya University, Chikusa-ku, 464-8602 Nagoya, Japan

¹¹ CNRS, IRAP, 9 Av. colonel Roche, BP 44346, 31028 Toulouse Cedex 4, France

¹² Department of Astronomy, University of Virginia, PO Box 400325, Charlottesville, VA 22904-4325, USA

¹³ National Radio Astronomy Observatory, 520 Edgemont Rd., Charlottesville, VA 22903, USA

¹⁴ Sterrewacht Leiden, Leiden University, PO Box 9513, 2300 RA Leiden, The Netherlands

¹⁵ National Astronomical Observatory of Japan, Mitaka, 181-8588 Tokyo, Japan

¹⁶ Space Telescope Science Institute, 3700 San Martin Dr., Baltimore, MD 21218, USA

¹⁷ Department of Physics and Astronomy, The Johns Hopkins University, 366 Bloomberg Center, 3400 N Charles St., Baltimore,
MD 21218, USA

¹⁸ Department of Physical Science, Graduate School of Science, Osaka Prefecture University, 1-1 Gakuen-cho, Naka-ku, Sakai,
599-8531 Osaka, Japan

¹⁹ NASA Goddard Space Flight Center, 8800 Greenbelt Rd., Greenbelt, MD 20771, USA

Received 9 January 2016 / Accepted 12 June 2016

ABSTRACT

We present *Herschel* SPIRE Fourier Transform Spectrometer (FTS) observations of N159W, an active star-forming region in the Large Magellanic Cloud (LMC). In our observations, a number of far-infrared cooling lines, including carbon monoxide (CO) $J = 4 \rightarrow 3$ to $J = 12 \rightarrow 11$, [CI] 609 μm and 370 μm , and [NII] 205 μm , are clearly detected. With an aim of investigating the physical conditions and excitation processes of molecular gas, we first construct CO spectral line energy distributions (SLEDs) on ~ 10 pc scales by combining the FTS CO transitions with ground-based low- J CO data and analyze the observed CO SLEDs using non-LTE (local thermodynamic equilibrium) radiative transfer models. We find that the CO-traced molecular gas in N159W is warm (kinetic temperature of 153–754 K) and moderately dense (H_2 number density of $(1.1\text{--}4.5) \times 10^3 \text{ cm}^{-3}$). To assess the impact of the energetic processes in the interstellar medium on the physical conditions of the CO-emitting gas, we then compare the observed CO line intensities with the models of photodissociation regions (PDRs) and shocks. We first constrain the properties of PDRs by modeling *Herschel* observations of [OI] 145 μm , [CII] 158 μm , and [CI] 370 μm fine-structure lines and find that the constrained PDR components emit very weak CO emission. X-rays and cosmic-rays are also found to provide a negligible contribution to the CO emission, essentially ruling out ionizing sources (ultraviolet photons, X-rays, and cosmic-rays) as the dominant heating source for CO in N159W. On the other hand, mechanical heating by low-velocity C-type shocks with $\sim 10 \text{ km s}^{-1}$ appears sufficient enough to reproduce the observed warm CO.

Key words. ISM: molecules – Magellanic Clouds – galaxies: ISM – infrared: ISM

* *Herschel* is an ESA space observatory with science instruments provided by European-led Principal Investigator consortia and with important participation from NASA.

** The final reduced *Herschel* data (FITS files) are only available at the CDS via anonymous ftp to cdsarc.u-strasbg.fr (130.79.128.5) or via <http://cdsarc.u-strasbg.fr/viz-bin/qcat?J/A+A/596/A85>

1. Introduction

Star formation exclusively occurs in molecular clouds, the densest component of the interstellar medium (ISM; e.g., [Kennicutt & Evans 2012](#)). The main constituent of these molecular clouds is molecular hydrogen (H_2) which is, unfortunately, not directly observable in the typical conditions of cold molecular gas owing to its symmetric, homonuclear nature. The strong rotational transitions of carbon monoxide (^{12}CO ; simply CO hereafter) at mm and sub-mm wavelengths have, instead, been used as common tracers of molecular gas. In particular, CO rotational lines have a wide range of critical densities, making them accessible probes of the physical conditions of molecular gas in diverse environments (e.g., kinetic temperature $T_k \sim 10\text{--}1000$ K and hydrogen density $n \sim 10^3\text{--}10^8$ cm $^{-3}$).

The diagnostic power of CO rotational transitions has been exploited considerably further since the advent of the ESA *Herschel* Space Observatory ([Pilbratt et al. 2010](#)). In combination with ground-based telescope data, Photodetector Array Camera and Spectrometer (PACS; [Poglitsch et al. 2010](#)), Spectral and Photometric Imaging Receiver (SPIRE; [Griffin et al. 2010](#)), and Heterodyne Instrument for the Far Infrared (HIFI; [de Graauw et al. 2010](#)) spectroscopic observations have enabled us to construct CO spectral line energy distributions (SLEDs) from the upper level $J_u = 1$ to 50. In recent years, *Herschel*-based CO SLEDs have been extensively examined for a wide range of Galactic (e.g., photodissociation regions (PDRs): [Habart et al. 2010](#); [Köhler et al. 2014](#); [Pon et al. 2014](#); [Stock et al. 2015](#); protostars: [Larson et al. 2015](#)) and extragalactic sources (e.g., infrared (IR)-bright galaxies: [Rangwala et al. 2011](#); [Kamenetzky et al. 2012](#); [Meijerink et al. 2013](#); [Pellegrini et al. 2013](#); [Greve et al. 2014](#); [Lu et al. 2014](#); [Papadopoulos et al. 2014](#); [Rosenberg et al. 2014](#); [Schirm et al. 2014](#); [Mashian et al. 2015](#); [Wu et al. 2015b](#); Seyfert galaxies: [van der Werf et al. 2010](#); [Hailey-Dunsheath et al. 2012](#); [Israel et al. 2014](#)), revealing the ubiquitous presence of warm molecular gas ($T_k \gtrsim 100$ K). Various heating sources, e.g., ultraviolet (UV) photons, X-rays, and cosmic-rays, have been invoked to explain the properties of this warm molecular gas and the emerging picture is that non-ionizing sources, such as mechanical heating (e.g., shocks driven by merging activities, stellar winds, and supernova explosions), must play a critical role.

In this paper, we aim at probing the physical conditions and excitation processes of molecular gas traced by CO emission in detail on individual molecular cloud scales. To do so, we study N159W, an active star-forming region in the Large Magellanic Cloud (LMC), largely based on *Herschel* PACS and SPIRE observations. The LMC is an excellent laboratory for our study for the following reasons. First of all, the proximity of the LMC (distance of ~ 50 kpc; e.g., [Pietrzyński et al. 2013](#)) enables us to perform high-resolution observations of spatially-resolved molecular clouds. In addition, the LMC is located at high Galactic latitude and has an almost face-on orientation (inclination angle of $\sim 35^\circ$; e.g., [van der Marel & Cioni 2001](#)), providing a view with less confusion and low interstellar extinction.

N159W is one of the three prominent molecular clouds in the HII region complex N159 (Fig. 1) and its stellar and gas contents have been extensively studied at multiple wavelengths. For example, previous optical and near IR studies have identified a large number of O- and B-type stars, embedded young stellar objects (YSOs), and ultracompact HII regions (e.g., [Jones et al. 2005](#); [Fariña et al. 2009](#); [Chen et al. 2010](#); [Carlson et al. 2012](#)), suggesting that N159W is one of the most intense star-forming regions in the LMC. As the brightest CO(1–0) peak in the

LMC (e.g., [Johansson et al. 1994](#); [Fukui et al. 1999](#); [Wong et al. 2011](#)), N159W has been frequently targeted for radio, mm, and sub-mm observations as well. The Australia Telescope Compact Array (ATCA) and the Atacama Large Millimeter/submillimeter Array (ALMA) have provided the sharpest view of molecular gas so far ([Seale et al. 2012](#); [Fukui et al. 2015](#)), revealing the complex filamentary distributions of CO(2–1), $^{13}CO(2-1)$, HCO $^+(1-0)$, and HCN(1–0). The presence of high excitation molecular gas was hinted at by CO(4–3), CO(6–5), and CO(7–6) observations by [Bolatto et al. \(2005\)](#), [Pineda et al. \(2008\)](#), [Mizuno et al. \(2010\)](#), and [Okada et al. \(2015\)](#).

Besides the extensive observations at multiple wavelengths, the presence of various energetic sources makes N159W an ideal target for our study. As described in the previous paragraph, numerous OB-type stars and YSOs exist in the region and they can produce UV photons and strong stellar outflows. In addition, the nearby black hole binary LMC X-1, the most luminous X-ray source in the LMC (X-ray luminosity of $\sim 10^{38}$ erg s $^{-1}$; [Schlegel et al. 1994](#)), can have a substantial influence on the surrounding ISM. Compared to UV photons, X-rays penetrate deeper into molecular clouds while dissociating fewer molecules. As a result, X-rays produce larger column densities of warm molecular gas for a given irradiation energy (e.g., [Meijerink & Spaans 2005](#)). The supernova remnant (SNR) J0540.0–6944 and its expanding shell are located just ~ 75 pc from N159W (e.g., [Chu et al. 1997](#); [Williams et al. 2000](#)) and can be another source of heating. Last but not least, a number of studies have indicated that the “molecular ridge” where N159W is located may have been exposed to large-scale energetic events driven by multiple supernova explosions, tidal force, and/or ram pressure. The molecular ridge is the largest molecular concentration in the LMC, comprising $\sim 30\%$ of the total molecular mass in the galaxy (e.g., [Mizuno et al. 2001](#)). The distribution of star formation across the ridge is quite intriguing, increasing from south to north toward the starbursting 30 Doradus region, and this has led several authors to suggest sequential star formation. For example, [de Boer et al. \(1998\)](#) proposed that the motion of the LMC through the hot halo gas of the Milky Way created bow shocks at the leading edge, consequently triggering the sequential star formation. This leading edge of the LMC corresponds to the southeastern HI overdensity region, which appears to merge into the Small Magellanic Cloud (SMC) through the Magellanic Bridge connecting the two Magellanic Clouds (e.g., [Kim et al. 1998](#); [Putman et al. 2003](#)). Since the Magellanic Bridge has been considered to be formed through gravitational interactions between the two Magellanic Clouds (e.g., [Bekki & Chiba 2007](#); [Besla et al. 2012](#)), this hints that the tidal force could be at work in the HI overdensity region. The HI overdensity region has also been shown to harbour several supergiant and giant HI shells (e.g., [Kim et al. 1998, 1999](#)), suggesting that powerful supernova explosions from multiple OB associations have injected a large amount of mechanical energy into the surrounding ISM. In Fig. 1, we present three-color composite and HI column density images of N159W and its surrounding regions.

This paper is organized in the following way. First, we provide a description of the multiwavelength datasets used in our study (Sect. 2). Next, we discuss spectral line detection in our *Herschel* SPIRE Fourier Transform Spectrometer (FTS) observations (Sect. 3) and derive the physical properties of molecular gas by modeling CO lines with the non-LTE radiative transfer code RADEX ([van der Tak et al. 2007](#); Sect. 4). We then employ theoretical models of PDRs and shocks to examine the excitation conditions of CO in N159W (Sect. 5) and finally summarize our conclusions (Sect. 6).

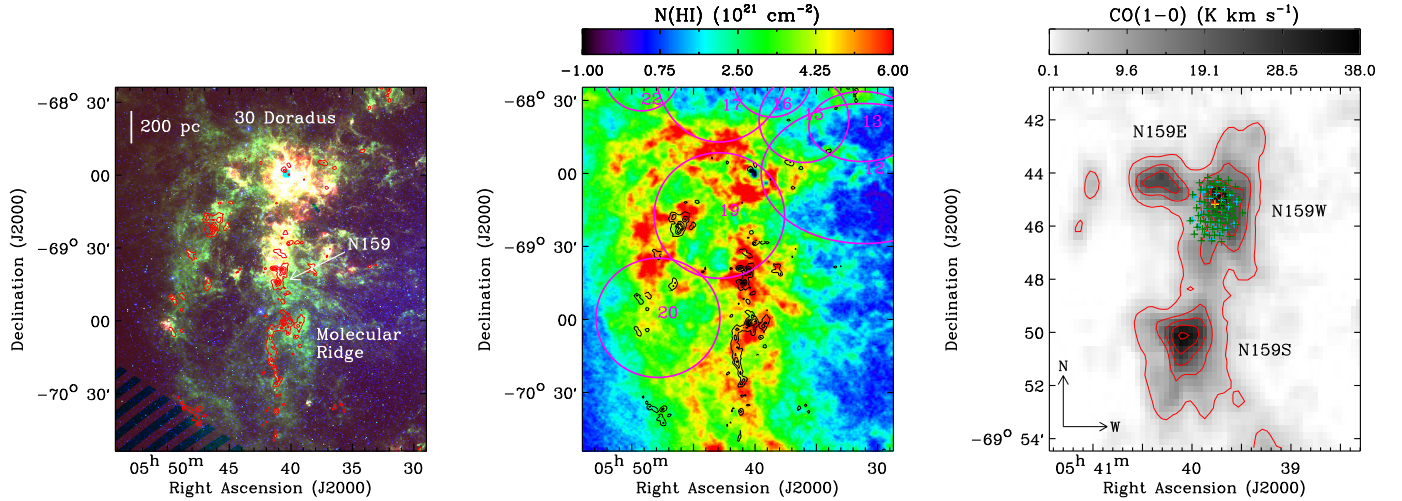


Fig. 1. *Left panel:* three-color composite image of the HII region complex N159 and its surrounding environment (*Spitzer* 3.6 μm /8 μm /24 μm in blue/green/red; Meixner et al. 2006). The CO(1–0) integrated intensity from the MAGMA survey (Wong et al. 2011) is shown as the red contours with levels ranging from 10% to 90% of the peak (39.5 K km s^{−1}) in 20% steps. *Middle panel:* HI column density image from Kim et al. (1998) with the same MAGMA CO contours as shown in the left panel (now in black). Several of the supergiant HI shells, identified by Kim et al. (1999) (clockwise from left: SGSs 22, 17, 16, 15, 13, 12, 19, and 20), are shown as the purple circles. This large-scale HI structure, where the molecular ridge is embedded, corresponds to the southeastern HI overdensity region in the LMC. *Right panel:* CO(1–0) integrated intensity image of N159 with the same contours as presented in the left panel. The locations of the SLW and SSW detectors are shown as the blue and green crosses, while the central detectors for the first jiggle observation (SLWC3 and SSWD4) are in yellow and orange. All these detectors are also shown in Fig. 3. Finally, the three prominent sub-regions in N159 are labeled.

2. Data

In this section, we describe the data in our study and summarize their main parameters (e.g., rest wavelength, FWHM, 1σ uncertainty in the integrated intensity, luminosity, etc.; Table 1).

2.1. *Herschel* SPIRE spectroscopic data

2.1.1. Observations

N159W was observed with the SPIRE FTS in the high spectral resolution ($\Delta f \sim 1.2$ GHz), intermediate spatial sampling mode. The FTS has two spectrometer arrays, SPIRE Long Wavelength (SLW) and SPIRE Short Wavelength (SSW), which cover wavelength ranges of 303–671 μm and 194–313 μm respectively. The FTS beam profile changes with wavelength and cannot be characterized by a simple Gaussian function due to the multi-moded nature of feedhorn coupled detectors (Makiwa et al. 2013). The FTS beam size varies from 17'' to 42'' (corresponding to 4–10 pc at the distance of the LMC; Wu et al. 2015b) and is presented in Table 1. The SLW and SSW arrays consist of 19 and 37 detectors respectively, which are arranged in a hexagonal pattern covering a $\sim 3' \times 3'$ area. In the intermediate spatial sampling mode, the SLW and SSW are moved to four jiggling positions with $\sim 28''$ and $\sim 16''$ spacings respectively. The locations of all detectors are shown in Figs. 1 and 3. Note that our final maps are sub-Nyquist sampled because of the detector spacing that roughly corresponds to the FTS beam size. The observations were performed on January 8, 2013 with a total integration time of 5707 s (Obs. ID: 1342259066; PI: S. Hony).

2.1.2. Data processing and map-making

We process the FTS data using the *Herschel* Interactive Processing Environment (HIPE) version 11.0.2825 and the SPIRE calibration version 11.0 (Fulton et al. 2010; Swinyard et al. 2014).

The calibration was obtained from measurements of Uranus and its uncertainty was estimated to be $\sim 10\%$ (SPIRE Manual)¹

To derive integrated intensity images and their uncertainties, we employ the data reduction script by Wu et al. (2015b), which was recently used to successfully generate FTS cubes for M 83. We first start off by performing line measurement of point source calibrated spectra for each transition. As an example, the spectra from the central SLW and SSW detectors are presented in Fig. 2, with the locations of the spectral lines observed with the SPIRE FTS. In our line measurement, a combination of parabola (continuum) and sinc (emission) functions is used to fit a spectral line for the frequency range of $\nu_{\text{line}} \pm 15$ GHz, where ν_{line} is the rest frequency of the line. The continuum subtracted spectra are then projected onto a common grid covering a $5' \times 5'$ area with a pixel size of 15'' (roughly corresponding to the jiggle spacing of the SSW observations) to construct a spectral cube. The spectrum for each pixel is calculated as the $(1/\sigma_p^2)$ -weighted sum of overlapping spectra, where σ_p is the 1σ uncertainty provided by the pipeline. The overlapping spectra are scaled in proportion to their covering areas in the pixel before the summation. Finally, the integrated intensity (I_{CO} , I_{Cl} , or I_{NH}) is derived by performing line measurement of the constructed spectral cube and its uncertainty (σ_f) is obtained by adding two errors in quadrature, $\sigma_f = \sqrt{\sigma_s^2 + \sigma_c^2}$, where σ_s is the statistical error based on the residual from line measurement and σ_c is the calibration error of 10%.

In this paper, we combine the FTS data with other tracers of gas and dust (Sects. 2.2–2.4). To compare them at a common resolution, we smooth the FTS maps to 42'' resolution (~ 10 pc at the LMC distance), which corresponds to the FWHM for the CO(4–3) transition, by convolving with proper kernels. These kernels were generated by Wu et al. (2015b) based on the fitting of a two-dimensional Hermite-Gaussian function to the FTS beam profiles, essentially following the method by

¹ http://herschel.esac.esa.int/Docs/SPIRE/html/spire_om.html

Table 1. Spectral lines and dust continuum emission in our study.

Species	Transition	Rest wavelength ^a (μm)	E_u^a (K)	n_{crit}^b (cm^{-3})	$FWHM^c$ ($''$)	$\sigma_{s,\text{med}}^{d,g,h}$ ($10^{-11} \text{ W m}^{-2} \text{ sr}^{-1}$)	$\sigma_{f,\text{med}}^{e,g,h}$ ($10^{-11} \text{ W m}^{-2} \text{ sr}^{-1}$)	Luminosity ^{f,g} (L_\odot)
¹² CO	$J = 1-0$	2600.8	6	4.7×10^2	45	0.1	0.8	0.9 ± 0.1
¹² CO	$J = 3-2$	867.0	33	1.5×10^4	22	1.4	25.1	33.5 ± 1.9
¹² CO	$J = 4-3$	650.3	55	3.7×10^4	42	15.3	29.4	67.8 ± 2.2
¹² CO	$J = 5-4$	520.2	83	7.2×10^4	34	11.6	34.6	88.5 ± 2.6
¹² CO	$J = 6-5$	433.6	116	1.3×10^5	29	6.6	36.9	101.5 ± 3.0
¹² CO	$J = 7-6$	371.7	155	2.0×10^5	33	6.3	32.5	86.5 ± 2.6
¹² CO	$J = 8-7$	325.2	199	2.9×10^5	33	17.2	29.4	71.5 ± 2.6
¹² CO	$J = 9-8$	289.1	249	4.0×10^5	19	14.7	22.6	48.7 ± 1.7
¹² CO	$J = 10-9$	260.2	304	5.3×10^5	18	18.3	22.7	33.4 ± 1.5
¹² CO	$J = 11-10$	236.6	365	7.0×10^5	17	20.6	23.2	24.3 ± 1.3
¹² CO	$J = 12-11$	216.9	431	9.0×10^5	17	17.9	23.2	18.9 ± 1.1
¹² CO	$J = 13-12$	200.3	503	1.1×10^6	17	27.1	27.9	–
[CI]	$^3P_1-^3P_0$	609.1	24	4.9×10^2	38	17.9	20.0	18.8 ± 1.2
[CI]	$^3P_2-^3P_1$	370.4	62	9.3×10^2	33	6.3	17.4	48.8 ± 1.5
[CII]	$^2P_{3/2}-^2P_{1/2}$	157.7	91	2.7×10^3	12	368.8	9439.1	3907.2 ± 399.9
[OI]	$^3P_0-^3P_1$	145.5	327	1.5×10^5	12	88.1	622.7	250.3 ± 25.4
[OI]	$^3P_1-^3P_2$	63.2	228	9.7×10^5	10	354.5	6444.5	2435.1 ± 248.9
[OIII]	$^3P_1-^3P_0$	88.4	163	5.0×10^2	10	544.8	1.1×10^4	5460.5 ± 600.8
[NII]	$^3P_1-^3P_0$	205.2	70	4.5×10^1	17	27.5	42.5	99.2 ± 3.5
L_{FIR}	–	60–200	–	–	42	–	3.9×10^4	$(3.3 \pm 0.1) \times 10^5$
L_{TIR}	–	3–1000	–	–	42	–	8.1×10^4	$(7.5 \pm 0.1) \times 10^5$

Notes. ^(a) Data from Leiden Atomic and Molecular Database (except for [NII] and [OIII], whose data come from Carilli & Walter 2013). ^(b) Critical density (CO data from Walker et al. 2015 and the rest from Tielens 2005). For the CO, [CI], [CII], and [OI] lines, the critical densities are evaluated at the kinetic temperature of 100 K. ^(c) Angular resolution of the original data. ^(d) Median σ_s in the integrated intensity at $42''$ resolution (σ_s = statistical 1σ uncertainty). ^(e) Median σ_f in the integrated intensity at $42''$ resolution (σ_f = final 1σ uncertainty; statistical and calibration errors added in quadrature). ^(f) Luminosity derived by integrating over all pixels with $S/N_s > 5$ at $42''$ resolution. ^(g) Except for CO(1–0) at $45''$ resolution. ^(h) For CO(1–0) and CO(3–2), the conversion factors of 1.6×10^{-12} and 4.2×10^{-11} are used to convert K km s^{-1} into $\text{W m}^{-2} \text{sr}^{-1}$. ^(d,e,f) Different spatial areas are considered for the estimates: $\sim 1.0' \times 1.5'$ for the [CII], [OI], and [OIII] transitions and $\sim 2.5' \times 2.5'$ for the rest.

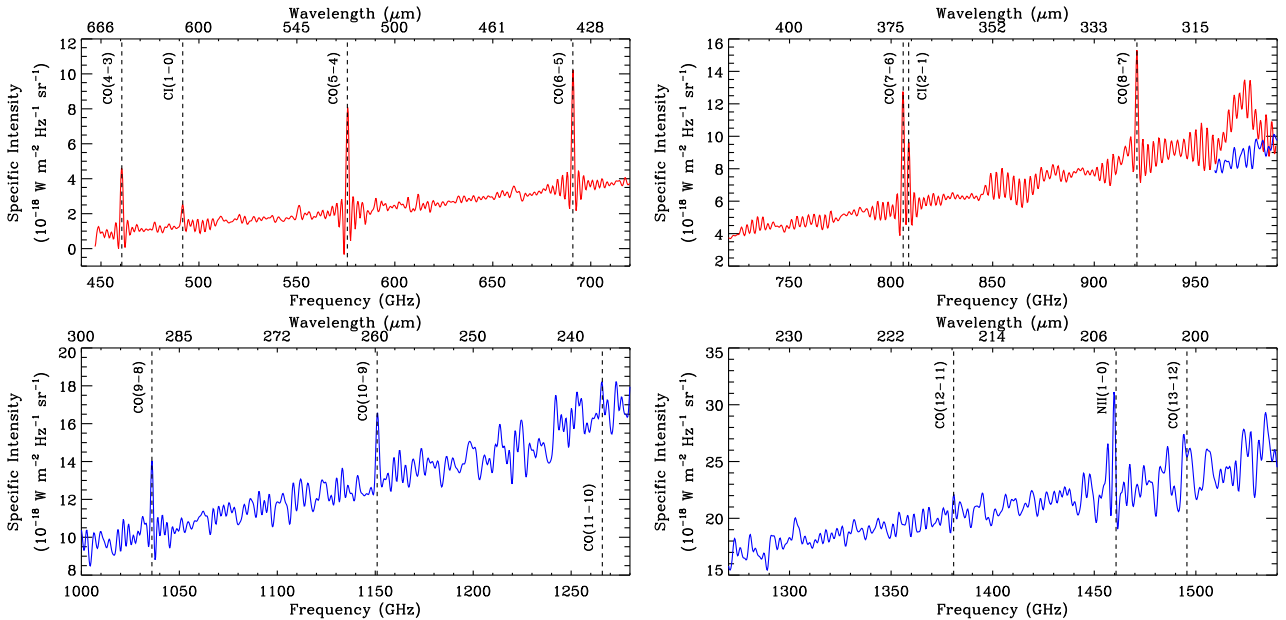


Fig. 2. Point source calibrated FTS spectra obtained with the two central detectors, SLWC3 (red) and SSWD4 (blue), for the first jiggle observation. The positions of the two detectors are shown as the yellow and orange crosses in Figs. 1 and 3 and the spectral lines observed with the SPIRE FTS are indicated as the black dashed lines.

Gordon et al. (2008). In addition, we rebin the smoothed maps to have a final pixel size of $30''$, which roughly corresponds to the jiggle spacing of the SLW observations. We present the resulting integrated intensity images in Fig. 3 and Appendix A and refer to Wu et al. (2015b) for details on the map-making procedure.

Finally, to cross-check our map-making procedure, we compare the FTS CO(4–3) integrated intensity image with NANTEN2 CO(4–3) observations at $38''$ resolution (Mizuno et al. 2010). For the comparison, we convolve the NANTEN2 data with a Gaussian kernel to have a final resolution of $42''$ and

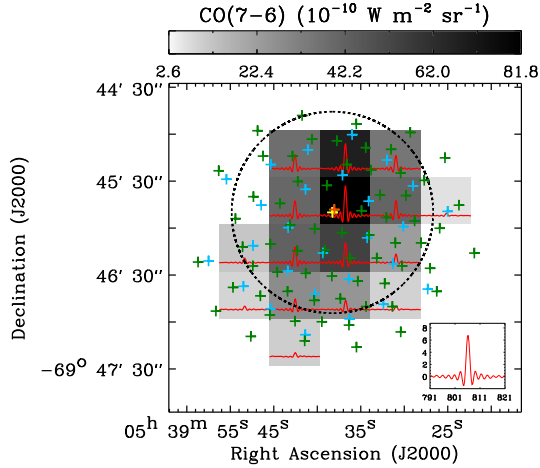


Fig. 3. CO(7–6) integrated intensity image at 42'' resolution (pixel size = 30''). In our FTS observations, CO(7–6) is one of the most sensitive transitions with the lowest median statistical uncertainty ($\sigma_{s,med}$; Table 1). The SLW and SSW arrays are shown as the blue and green crosses, except the central detectors for the first jiggle observation (SLWC3 and SSWD4) in yellow and orange. The spectra with the statistical signal-to-noise ratio S/N_s (integrated intensity divided by σ_s) > 5 are presented in red (our threshold for detection; Sect. 3.1) and their x -axis (in GHz) and y -axis (in $10^{-18} \text{ W m}^{-2} \text{ Hz}^{-1} \text{ sr}^{-1}$) ranges are shown in the *bottom right* corner with the spectrum of the pixel observed with SLWC3 and SSWD4. The black dashed circle delineates the 2' unvignetted field-of-view for FTS observations and almost all pixels are within this field-of-view. Note that we do have a spectrum for every detector and the blank pixels within the SLW coverage in the current image simply result from the rebinning process.

find that the FTS and NANTEN2 data are consistent within 1σ uncertainties: the ratio of the FTS to NANTEN2 data ranges from ~ 0.7 to ~ 1.2 , suggesting that our map-making procedure is accurate.

2.2. Herschel PACS spectroscopic data

N159W was observed with the PACS spectrometer on May 24, 2011, as part of the *Herschel* guaranteed time key project SHINING (PI: E. Sturm). The four fine-structure lines, [CII] 158 μm , [OI] 63 μm , [OI] 145 μm , and [OIII] 88 μm , were mapped in the unchopped scan mode (Obs. IDs: 1342222075 to 1342222084). As described in Poglitsch et al. (2010), the PACS spectrometer is an integral field spectrometer that consists of 25 (spatial) \times 16 (spectral) pixels. The spectrometer covers a wavelength range of 51–220 μm with a projected footprint of 5×5 spatial pixels (“spaxels”) on the sky (corresponding to a $\sim 47'' \times 47''$ field-of-view). The FWHM depends on wavelengths, ranging from $\sim 10''$ at 60 μm to $\sim 12''$ at 160 μm (PACS Manual)².

The PACS spectroscopic data are first reduced with the HIPE version 12.0.0 (Ott 2010) from Level 0 to Level 1. The Level 1 cubes (calibrated in both flux and wavelength) are then exported and processed with PACSman (Lebouteiller et al. 2012) to create integrated intensity images. Each spectrum is fitted with a combination of polynomial (baseline) and Gaussian (line) functions and the line fluxes of all spaxels are projected onto a grid with a size of $\sim 1' \times 2'$. The pixel size of $\sim 3''$ (corresponding to $\sim 1/3$ of the spaxel size) is chosen to recover the best spatial resolution possible. For the 1σ error in the integrated intensity, the uncertainty from map projection/line measurement (σ_s ;

provided by PACSman) and the calibration uncertainty of 22% (σ_c ; 10% for spaxel-to-spaxel variations and 12% for absolute calibration) are added in quadrature. We present final integrated intensity maps and a sample of PACS spectra in Figs. 4 and 5 and refer to Lebouteiller et al. (2012) and Cormier et al. (2015) for details on the data reduction and map-making procedures.

The limited spatial coverage of the PACS data, unfortunately, results in only several pixels to work with when the maps are smoothed and regridded to match the FTS resolution (42'') and pixel size (30''). The common region between the PACS and FTS data at 42'' resolution has a size of $\sim 1.0' \times 1.5'$ (e.g., Fig. 13) and all fine-structure transitions are clearly detected with the statistical signal-to-noise ratio S/N_s (integrated intensity divided by σ_s) > 5 (our threshold for line detection; Sect. 3.1).

2.3. Ground-based CO data

2.3.1. Mopra CO(1–0) data

We use the CO(1–0) data from the MAGellanic Mopra Assessment (MAGMA) survey (Wong et al. 2011). This survey targeted bright CO complexes that were previously identified from the NANTEN survey (Mizuno et al. 2001) and observed them with the 22 m Mopra telescope on 45'' scales. To estimate the CO(1–0) integrated intensity, each data cube was first smoothed to 90'' resolution and a mask was generated based on the 3σ level. The generated mask was then applied to the original cube and the CO(1–0) emission within the mask was integrated from $v_{LSR} = +200 \text{ km s}^{-1}$ to $+305 \text{ km s}^{-1}$. The uncertainty in the integrated intensity was derived by multiplying the root-mean-square (rms) noise per channel by the square root of the number of channels that contribute to the intensity map at that position. To take a systematic error into account, we combine this uncertainty with the calibration uncertainty of 25% (T. Wong, priv. comm.) and add them in quadrature. For the area that overlaps with the FTS coverage ($2.5' \times 2.5'$ in size; Fig. 7), the final uncertainty at 45'' resolution has a median of $\sim 5.3 \text{ K km s}^{-1}$ (Table 1) and the CO(1–0) transition is detected everywhere with $S/N_s > 5$.

2.3.2. ASTE CO(3–2) data

We use the CO(3–2) data obtained by Minamidani et al. (2008). Minamidani et al. (2008) observed N159 with the 10 m Atacama Submillimeter Telescope Experiment (ASTE) telescope at 22'' resolution. In order to derive the integrated intensity, we integrate the CO(3–2) emission from $v_{LSR} = +220 \text{ km s}^{-1}$ to $+250 \text{ km s}^{-1}$. This velocity range is slightly different from that used to estimate the CO(1–0) integrated intensity, but the discrepancy would not make a significant impact on the CO(3–2) integrated intensity considering that the spectra contain essentially noise beyond the velocity range of 220–250 km s^{-1} (e.g., Fig. 2 of Minamidani et al. 2008). The final uncertainty in the integrated intensity is then estimated in the same way as we do for CO(1–0): add the statistical error derived from the rms noise per channel and the calibration error of 20% (Minamidani et al. 2008) in quadrature. When smoothed to 42'' resolution and regridded to match the FTS data, the CO(3–2) observations have a median uncertainty of $\sim 5.9 \text{ K km s}^{-1}$ (Table 1) and $S/N_s > 5$ is achieved everywhere.

² http://herschel.esac.esa.int/Docs/PACS/html/pacs_om.html

³ In this paper, all velocities are quoted in the Local Standard of Rest (LSR) frame.

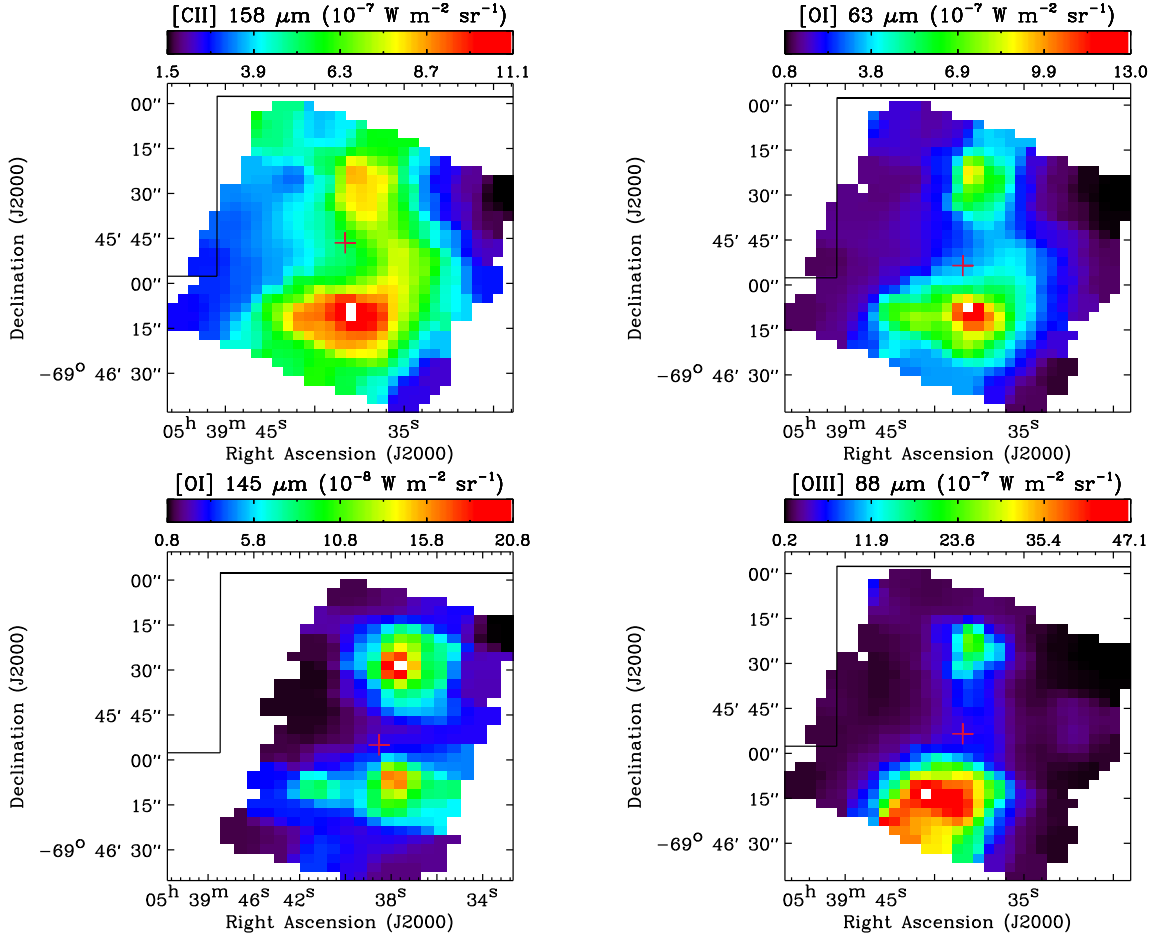


Fig. 4. Integrated intensity images of PACS fine-structure lines. The angular resolutions are $\sim 10''$ for [OI] $63 \mu\text{m}$ and [OIII] $88 \mu\text{m}$ and $\sim 12''$ for [OI] $145 \mu\text{m}$ and [CII] $158 \mu\text{m}$. The FTS coverage (e.g., Fig. 3) is indicated as the black solid line. Note that the PACS observations are spatially limited and hence only part of the FTS coverage is shown here. In each image, the location of the spaxel where an example spectrum is extracted is also overlaid as the red cross. This specific spaxel is chosen as the closest one to the FTS SLWC3 detector (yellow cross in Fig. 3). The extracted spectra are presented in Fig. 5.

2.4. Derived dust and IR continuum properties

We use the dust and IR continuum properties of N159W estimated following Galametz et al. (2013). To derive these properties, Galametz et al. (2013) applied the dust spectral energy distribution (SED) model by Galliano et al. (2011) to *Spitzer* (3.6, 4.5, 5.8, 8, 24, and $70 \mu\text{m}$) and *Herschel* (100, 160, 250, 350, and $500 \mu\text{m}$) photometric data (Meixner et al. 2006, 2013). The amorphous carbon (AC) composition was used for this purpose, as it was designed to consistently reproduce the *Herschel* broadband emission of the LMC. It is more emissive than the standard Draine & Li (2007) model. In essence, Galliano et al. (2011)'s approach is twofold: (1) modeling of dust SED for a single mass element of the ISM with uniform illumination and (2) synthesizing several mass elements to account for the variations in illumination conditions. In the SED fitting procedure, independent free parameters are the total dust mass (M_{dust}), PAH-to-dust mass ratio (f_{PAH}), index for the power-law distribution of starlight intensities (α_U), lower cut-off for the power-law distribution of starlight intensities (U_{min}), range of starlight intensities (ΔU), and mass of old stars (M_{star}). Based on these free parameters, the following properties can also be estimated (Fig. 6 and Table 1): far IR luminosity ($60\text{--}200 \mu\text{m}$; L_{FIR}), total IR luminosity ($3\text{--}1000 \mu\text{m}$; L_{TIR}), and dust temperature (T_{dust}). Galametz et al. (2013) derived all these parameters at

$36''$ resolution and estimated their uncertainties by performing MC simulations where the measured IR fluxes were perturbed based on 1σ errors and the SED fitting was repeated 20 times. In our study, we use the parameters estimated on $42''$ scales to match the FTS resolution. We refer to Galametz et al. (2013) and Galliano et al. (2011) for details on dust SED modeling.

3. Results

3.1. FTS line detection

We show the FTS spectra in Fig. 3 and Appendix A.1 and focus on CO and [CI] line detection in this section. A detailed analysis on the physical properties and excitation conditions of the CO-emitting gas will be presented in Sects. 4 and 5. Throughout this paper, we apply a threshold of $S/N_s > 5$ for line detection and categorize the CO transitions into three groups (e.g., Köhler et al. 2014): low- J for $J_u \leq 5$, intermediate- J for $6 \leq J_u \leq 9$, and high- J for $J_u \geq 10$ where J_u is the upper level J .

In N159W, FTS CO transitions with $J_u = 4\text{--}12$ are detected. These rotational lines have upper level energies of $E_u \sim 55\text{--}431 \text{ K}$ and critical densities of $n_{\text{crit}} \sim 10^4\text{--}10^6 \text{ cm}^{-3}$ (Table 1; Yang et al. 2010), suggesting that they are valuable probes of molecular gas over a range of density and temperature. To estimate the total CO luminosity, we add up the integrated

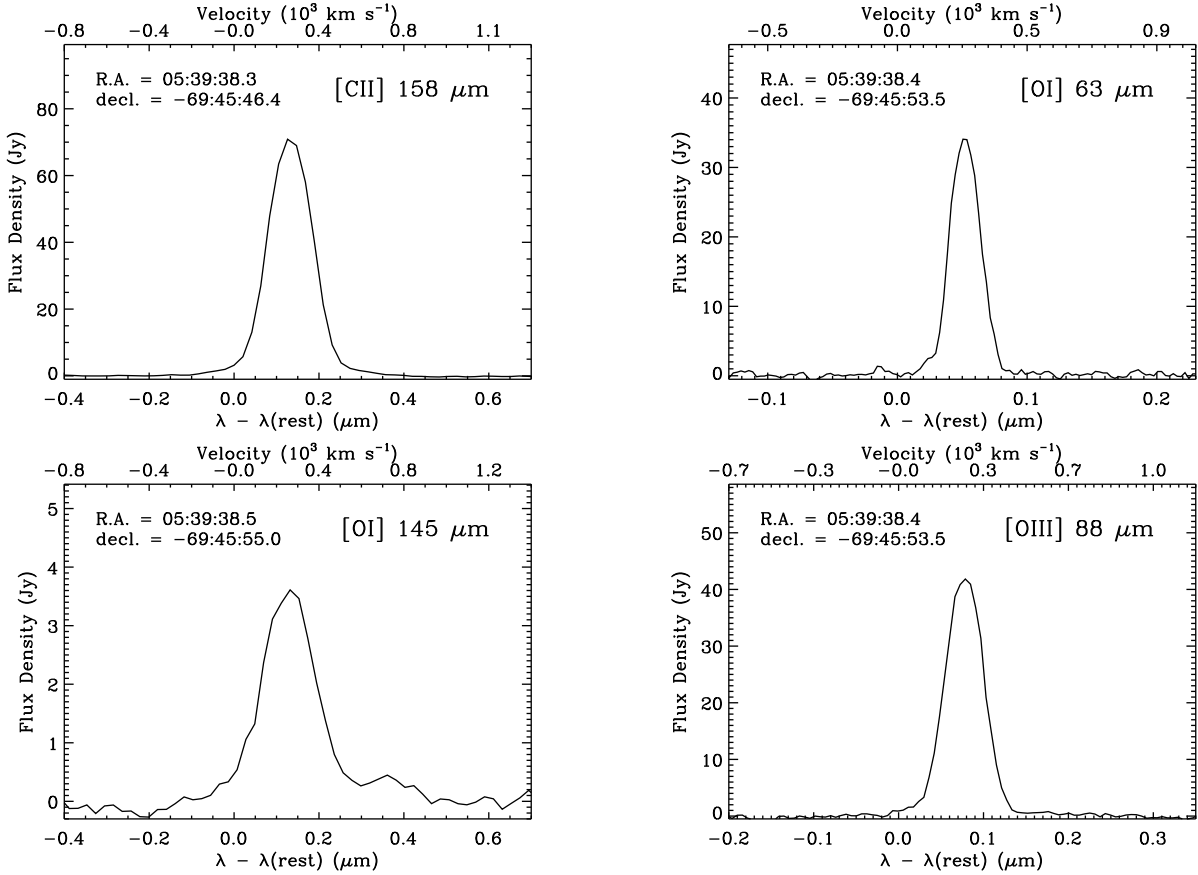


Fig. 5. Example PACS spectra. The location of the spaxel where each spectrum is extracted is indicated in the top left corner of each plot, as well as in Fig. 4 as the red cross.

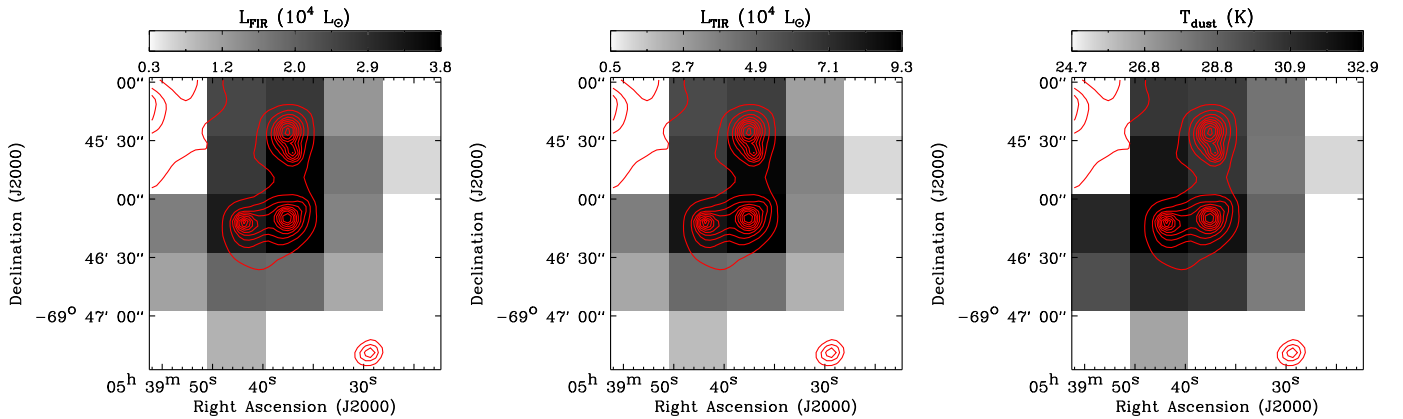


Fig. 6. Dust and IR continuum properties: far IR luminosity L_{FIR} (left), total IR luminosity L_{TIR} (middle), and dust temperature T_{dust} (right). All images are at $42''$ resolution with a pixel size of $30''$ and the *Spitzer* $24 \mu\text{m}$ emission at $6''$ resolution is overlaid as the red contours with levels ranging from 10% to 90% of the peak (2149 MJy sr^{-1}) in 10% steps.

intensities at $42''$ resolution over all pixels with $S/N_s > 5$ and provide the results in Table 1. We find the total CO luminosity of $L_{\text{CO}} = (575.5 \pm 6.8) L_{\odot}$ (including $J_u = 1, 3, 4, \dots, 12$), which is $\sim 8 \times 10^{-4}$ of the total IR luminosity. This total CO luminosity is dominated by the rotational lines with $4 \leq J_u \leq 8$ (low- J and intermediate- J) and the largest contribution ($\sim 20\%$) comes from the CO(6–5) transition. Note, however, that our estimate is limited up to $J_u = 12$. Considering that the observed CO SLEDs are relatively flat up to $J_u = 12$ for some pixels (Sect. 4.1), hinting at more CO emission at $J_u \geq 13$, the actual total CO luminosity is likely higher. To be specific, our

non-LTE radiative transfer modeling (Sect. 4.2) suggests that high- J transitions with $J_u \geq 13$ could contribute up to 8% of the total CO luminosity⁴.

Both atomic carbon fine-structure lines at $609 \mu\text{m}$ and $370 \mu\text{m}$ are detected in N159W. Their upper levels lie $\sim 24 \text{ K}$ and $\sim 62 \text{ K}$ above the ground state and their critical densities are low with $n_{\text{crit}} \sim 10^2\text{--}10^3 \text{ cm}^{-3}$ (Table 1; Launay & Roueff 1977). Under the typical conditions of PDRs (density $n \sim 0.5\text{--}10^7 \text{ cm}^{-3}$

⁴ This estimate is based on the assumption that there is no additional warm component emitting at $J_u \geq 13$.

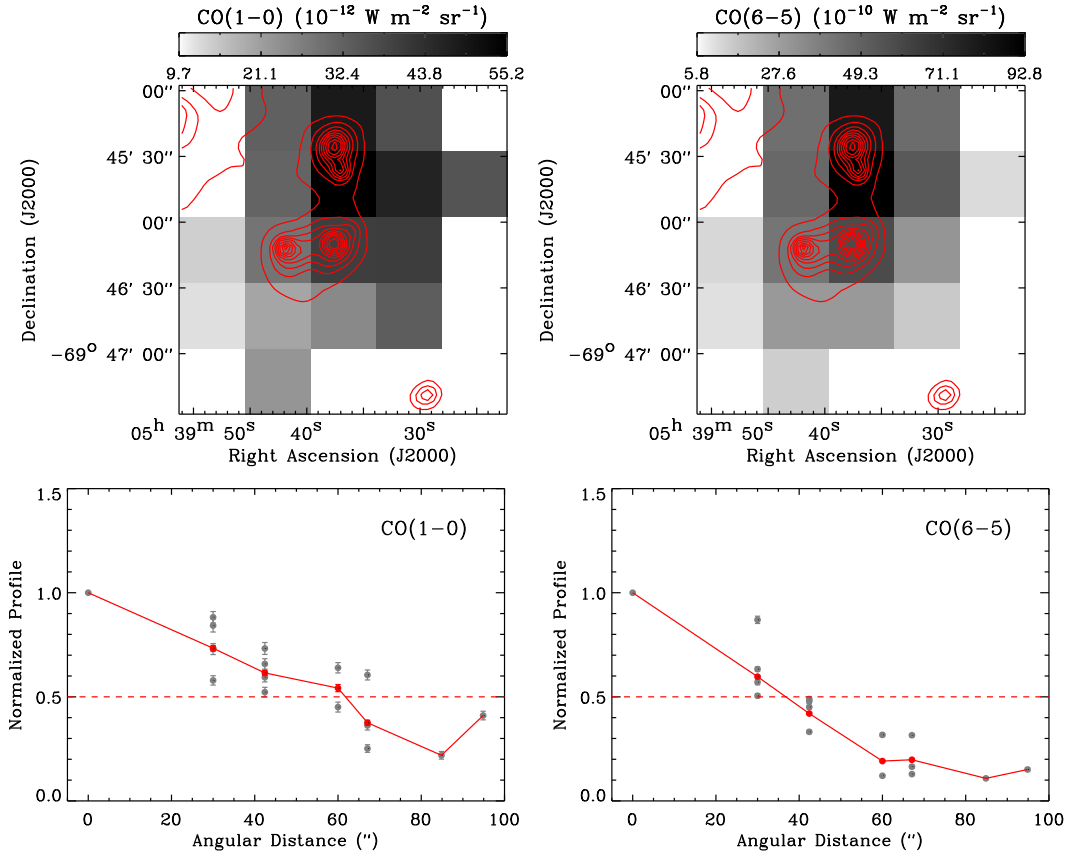


Fig. 7. *Top left:* CO(1–0) integrated intensity image at 45'' resolution. The *Spitzer* 24 μm emission at its original resolution of 6'' is overlaid in red with contour levels ranging from 10% to 90% of the peak (2149 MJy sr^{-1}) in 10% steps. *Top right:* same as the top left panel, but for CO(6–5). *Bottom left:* normalized CO(1–0) integrated intensity as a function of angular distance from its peak at (RA, Dec) = (05^h39^m37^s, –69°45'43''). The individual pixel values are shown as the gray circles and the $(1/\sigma_s^2)$ -weighted mean values are overplotted as the red circles when there is more than one data point in each angular distance bin. *Bottom right:* same as the bottom left panel, but for CO(6–5).

and temperature $T \sim 10\text{--}8000$ K; e.g., Hollenbach & Tielens 1997; Tielens 2005), the two [CI] lines therefore can be easily excited and thermalized. In N159W, the ratio of the 370 μm to 609 μm lines is $\sim 1.5\text{--}2.3$ for the regions where both lines are detected, which indicates optically thin emission (e.g., Pineda et al. 2008; Okada et al. 2015). As we do for the CO lines, we then estimate the total [CI] luminosity of $L_{\text{CI}} = (67.6 \pm 1.8) L_{\odot}$ by summing up the measured integrated intensities at 42'' resolution for the pixels with $S/N_s > 5$ (Table 1 for the luminosity of each transition). This corresponds to $\sim 9 \times 10^{-5}$ of the total IR luminosity. In comparison with CO, we find that the [CI] emission is much weaker. To be specific, the total CO-to-[CI] luminosity ratio varies from ~ 5 to ~ 18 with a median of ~ 9 .

3.2. Spatial distribution of the neutral gas traced by the CO and [CI] emission

In this section, we examine the spatial distribution of the neutral gas probed by the CO and [CI] emission on 42'' scales (~ 10 pc at the LMC distance). First of all, we find that the CO and [CI] integrated intensities peak at comparable locations, (RA, Dec) \sim (05^h39^m40^s, –69°45'30''). These peaks are adjacent to the peak of the *Spitzer* 24 μm emission (Fig. 7), which traces the warm dust heated by young stars. To quantify the spatial distribution of neutral gas, we derive a radial profile for each CO and [CI] transition and measure the radius at which the profile reaches half its maximum. As examples, CO(1–0) and CO(6–5) radial profiles are presented in Fig. 7. We show individual

pixel values as gray circles, while overplotting $(1/\sigma_s^2)$ -weighted values as red circles when there is more than one data point in each angular distance bin. In general, we find that intermediate- J and high- J transitions are more compact than low- J transitions. To be specific, the width at half maximum is $\sim 42''\text{--}60''$ for the low- J CO lines ($J_u \leq 5$), while not resolved ($< 42''$) for the intermediate- J and high- J CO lines ($J_u \geq 6$). Similar results were found in the FTS observations of Galactic PDRs, Orion Bar and NGC 7023 (Habart et al. 2010; Köhler et al. 2014). We also find that the [CI] 609 μm and 370 μm transitions are as compact as the CO lines with $J_u \geq 6$. Note, however, that our radial profile analysis is somewhat limited due to the incomplete coverage of the FTS maps (e.g., blank pixels at the edge) and large-scale observations are hence required to study the spatial distribution of the CO and [CI] emission more accurately.

4. Physical properties of the CO-emitting gas

4.1. Observed CO SLEDs

We present the observed CO SLEDs from $J_u = 1$ to 13 ($J_u = 2$ not included) in Fig. 8. To construct the CO SLED on a pixel-by-pixel basis, we use the integrated intensity images smoothed to the common resolution of 42'' and apply a threshold of $S/N_s > 5$ for line detection. Our CO SLED image clearly shows regional variations in the shape of the CO SLEDs, indicating different physical conditions of the CO-emitting gas. For example, the location of the peak and the slope beyond the peak are sensitive

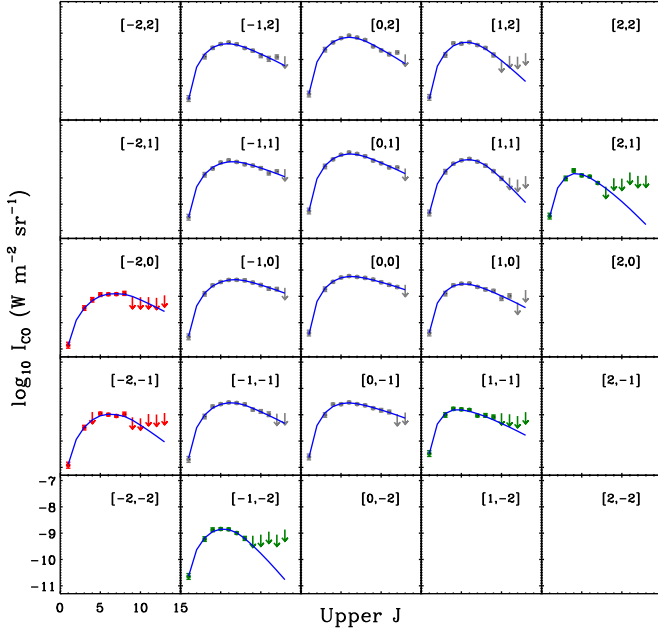


Fig. 8. CO SLEDs for $J_u = 1, \dots, 13$ ($J_u = 2$ not included). In this image, the pixels correspond to the individual data points ($30''$ in size) in our FTS maps at $42''$ resolution and the pair of numbers in the top right corner of each pixel shows a location relative to the center of the FTS coverage ($[0, 0]$ is $[RA, Dec] = [05^h 39^m 37^s, -69^\circ 46' 13'']$). The circles represent detected CO transitions and the downward arrows show upper limits based on $5\sigma_s$. Most of the observed CO SLEDs show peak at $J_u \geq 6$ (gray), while some pixels have peaks that are uncertain (red) or occur at the transitions lower than $J_u = 6$ (green). Finally, the best-fit RADEX models determined in Sect. 4.2 are overlaid in blue.

to the density and temperature, while the CO column density determines the line intensity magnitude. In N159W, most of the observed CO SLEDs peak at $J_u \geq 6$ (gray in Fig. 8; ten pixels at $J_u = 6$ and one pixel at $J_u = 7$), while some show peaks that are uncertain due to non-detections (red; two pixels) or occur at the transitions lower than $J_u = 6$ (green; one pixel at $J_u = 5$ and two pixels at $J_u = 4$).

It is interesting to notice that the CO SLEDs with peaks at $J_u \leq 5$ are all located at the edge of our FTS maps, some distance away from the active star-forming regions. In addition, the slope of each CO SLED beyond its peak spatially changes. To quantify how different the slopes are, we compute the “high- J slope” by $\Delta I_{CO, \text{norm}} = [I_{CO}(J_p + 3) - I_{CO}(J_p)] / I_{CO}(J_p)$, where $I_{CO}(J_p)$ is the integrated intensity of the peak transition J_p and $I_{CO}(J_p + 3)$ is the integrated intensity of the $J_p + 3$ transition (Fig. 9). By definition, the high- J slope is always negative and a smaller value represents a steeper decrease. The $J_p + 3$ transition is chosen here to calculate the high- J slope for all pixels except for those two whose peaks are uncertain. We find that the high- J slope changes by a factor of three across N159W. In particular, the two pixels corresponding to the active star-forming regions at $(RA, Dec) \sim (05^h 39^m 40^s, -69^\circ 46' 10'')$ (traced by the *Spitzer* $24 \mu\text{m}$ emission in Fig. 9) have the flattest CO SLEDs with $\Delta I_{CO, \text{norm}} \sim -0.3$ while the pixels at the northwest edge of our FTS maps show the steepest decrease with $\Delta I_{CO, \text{norm}} \sim -0.7$. A similar approach was recently adopted in Rosenberg et al. (2015), where the parameter $\alpha = [L_{CO}(J = 11-10) + L_{CO}(J = 12-11) + L_{CO}(J = 13-12)] / [L_{CO}(J = 5-4) + L_{CO}(J = 6-5) + L_{CO}(J = 7-6)]$ was used to categorize the CO SLEDs of 29 (ultra)luminous infrared galaxies (U)LIRGs). Almost an order of magnitude variation in the α parameter was found, confirming the diverse

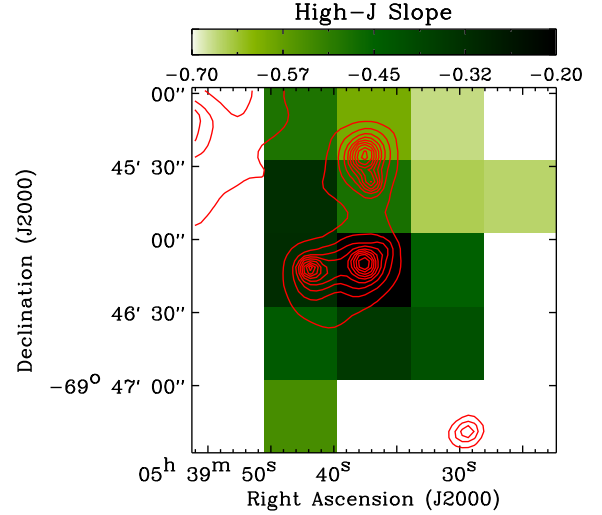


Fig. 9. High- J slope image overlaid with the $24 \mu\text{m}$ emission contours. Note that the two pixels whose CO SLEDs do not have clear peaks (red in Fig. 8) are masked here.

CO SLEDs found for many Galactic and extragalactic sources (e.g., Habart et al. 2010; van der Werf et al. 2010; Köhler et al. 2014; Kamenetzky et al. 2014; Mashian et al. 2015).

4.2. Non-LTE modeling

We analyze the observed CO SLEDs using the non-LTE radiative transfer code RADEX (van der Tak et al. 2007). To compute the intensities of atomic and molecular lines, RADEX solves the radiative transfer equation based on the escape probability method. By assuming that the spectral lines are produced in an isothermal and homogeneous medium, this simple model can then be used to constrain the physical conditions of the medium, e.g., kinetic temperature, density, and column density of each species.

To model the intensity of each CO transition, we consider a grid of the following input parameters: kinetic temperature $T_k = 10-10^3$ K, H_2 density $n(\text{H}_2) = 10^2-10^5 \text{ cm}^{-3}$, CO column density $N(\text{CO}) = 10^{15}-10^{20} \text{ cm}^{-2}$, and beam filling factor $\Omega = 10^{-3}-1$. These input parameters are sampled uniformly in log space with 50 points, except for $N(\text{CO})$ where 100 points are used. In addition, we use the cosmic microwave background radiation temperature of 2.73 K and the FWHM linewidth of 10 km s^{-1} (based on Pineda et al. 2008; and Mizuno et al. 2010, where CO transitions up to $J = 7-6$ were spectrally resolved for N159W). In our modeling, we compare the observed integrated intensities (I_{obs}) with RADEX predictions scaled by the beam filling factor (ΩI_{mod}) and find the best-fit model with the minimum χ^2 where χ^2 is defined as

$$\chi^2 = \sum_{i=1}^{13} \left[\frac{I_{i, \text{obs}} - (\Omega I_{i, \text{mod}})}{\sigma_{i, \text{obs}}} \right]^2. \quad (1)$$

Here σ_{obs} is the uncertainty in the observed integrated intensity and the summation is done for the CO transitions from $J_u = 1$ to 13 ($J_u = 2$ not included) with $S/N_s > 5$. We start with fitting the CO lines with a single temperature component, which is simplistic considering that multiple ISM phases are likely mixed at our spatial resolution of $\sim 10 \text{ pc}$. Nevertheless, using one component would still provide average physical conditions of the phases in the beam.

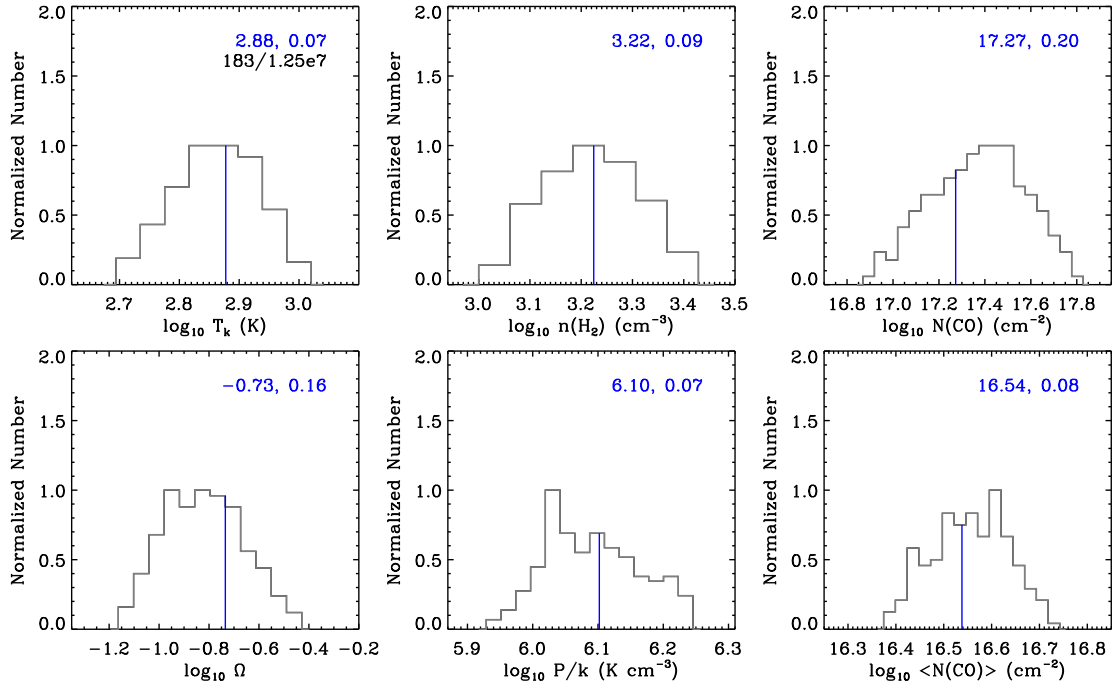


Fig. 10. Histograms of “good” parameters for the central pixel of our FTS maps ([0, 0] in Fig. 8; [RA, Dec] = [05^h39^m37^s, -69°46′13″]). To derive these histograms, the threshold of $\chi^2 \leq \text{minimum } \chi^2 + 4.7$ is applied to the calculated χ^2 distribution. Along with the log value of the best-fit parameter, the standard deviation of the χ^2 distribution measured in log space are shown in blue in the top right corner of each plot. The corresponding blue line of each histogram represents the best-fit parameter. Finally, the number in black in the T_k plot is the ratio of the number of “good” models to the total number of RADEX models in our study. See Sect. 4.2 for details.

We determine the best-fit RADEX models for individual pixels and show them with the observed CO SLEDs in Fig. 8. To illustrate how to estimate the uncertainties in the best-fit parameters, we then show the histograms of “good” parameters for the central pixel of our FTS maps ([0, 0] in Fig. 8) in Fig. 10. To derive these histograms, we apply a threshold of $\chi^2 \leq \text{minimum } \chi^2 + 4.7$ to the calculated χ^2 distribution: $\Delta\chi^2 = 4.7$ is chosen for the 1σ confidence interval with four parameters (T_k , $n(\text{H}_2)$, $N(\text{CO})$, and Ω ; Press et al. 1992). In addition to the histograms of the four primary parameters, those of secondary parameters, thermal pressure $P = nT_k \simeq n(\text{H}_2)T_k$ and beam-averaged CO column density $\langle N(\text{CO}) \rangle = \Omega N(\text{CO})$, are presented. We calculate the upper and lower error bounds by measuring the standard deviation of each “good” parameter distribution in log space, while noting that the distributions of “good” parameters are not always symmetric around the best-fit values. Since the primary parameters are degenerate in our modeling (T_k with $n(\text{H}_2)$ and $N(\text{CO})$ with Ω)⁵, their products, P and $\langle N(\text{CO}) \rangle$, are better constrained in general. The images of the best-fit parameters are presented in Fig. 11 and their ranges and 1σ uncertainties are summarized in Table 2.

4.3. Spatial distributions of the best-fit parameters

Figure 11 shows how the properties of the CO-emitting gas vary across N159W. We summarize our findings as follows.

As for the primary parameters, T_k and $n(\text{H}_2)$ show quite uniform distributions (only a factor of two variations around the median values of 429 K and $2.2 \times 10^3 \text{ cm}^{-3}$), while $N(\text{CO})$ and Ω change by a factor of ~ 30 across the entire $\sim 40 \text{ pc} \times 40 \text{ pc}$

⁵ Higher temperatures and lower densities can produce the same intensity as lower temperatures and higher densities. The same thing applies to CO column densities and beam filling factors.

region. For example, Ω varies from 0.02 to 0.5, but again mostly around the median of 0.1 (Fig. 11). The estimated beam filling factor of ~ 0.1 suggests that the CO clumps in N159W are on average $\sim 9''$ in size ($\sim 2 \text{ pc}$ at the LMC distance). This is consistent with what high-resolution ALMA observations of $^{13}\text{CO}(1-0)$, $^{13}\text{CO}(2-1)$, and $^{12}\text{CO}(2-1)$ in N159W found (Fukui et al. 2015): the spatially resolved CO structures are roughly $\sim 10''$ in size.

An interesting trend is that the pixels with high kinetic temperatures ($\sim 500\text{--}754 \text{ K}$) and beam filling factors ($\sim 0.1\text{--}0.2$) coincide with the data points with the flattest CO SLEDs (Fig. 9), essentially tracing the massive star-forming regions. On the other hand, the CO column density distribution shows the opposite: the peak ($\sim (0.6\text{--}1) \times 10^{18} \text{ cm}^{-2}$) instead occurs at the southeast and northwest edges of our FTS coverage. We note, however, that the primary parameters are degenerate in our RADEX modeling and have relatively large 1σ uncertainties (e.g., Table 2), limiting our ability to examine the spatial distributions of the parameters more accurately.

As the primary parameters are not independent of each other, it is therefore their products (secondary parameters) that can be better constrained and interpreted more straightforwardly. We find that both the thermal pressure and beam-averaged CO column density distributions are quite uniform with only a factor of four variations over our whole coverage. Their median values are $9.5 \times 10^5 \text{ K cm}^{-3}$ and $3.0 \times 10^{16} \text{ cm}^{-2}$ respectively.

In summary, the excellent agreement between the RADEX models and our CO SLEDs (Fig. 8) suggests that the CO lines up to $J = 12\text{--}11$ observed on $\sim 10 \text{ pc}$ scales are on average produced by a single temperature component. Our modeling shows that this component can be characterized by high thermal pressures of $\sim 9.5 \times 10^5 \text{ K cm}^{-3}$ and moderate beam-averaged CO column densities of $\sim 3.0 \times 10^{16} \text{ cm}^{-2}$ whose distributions are uniform across the $\sim 40 \text{ pc} \times 40 \text{ pc}$ region. Considering the good fit with the single temperature component, we do not attempt to add

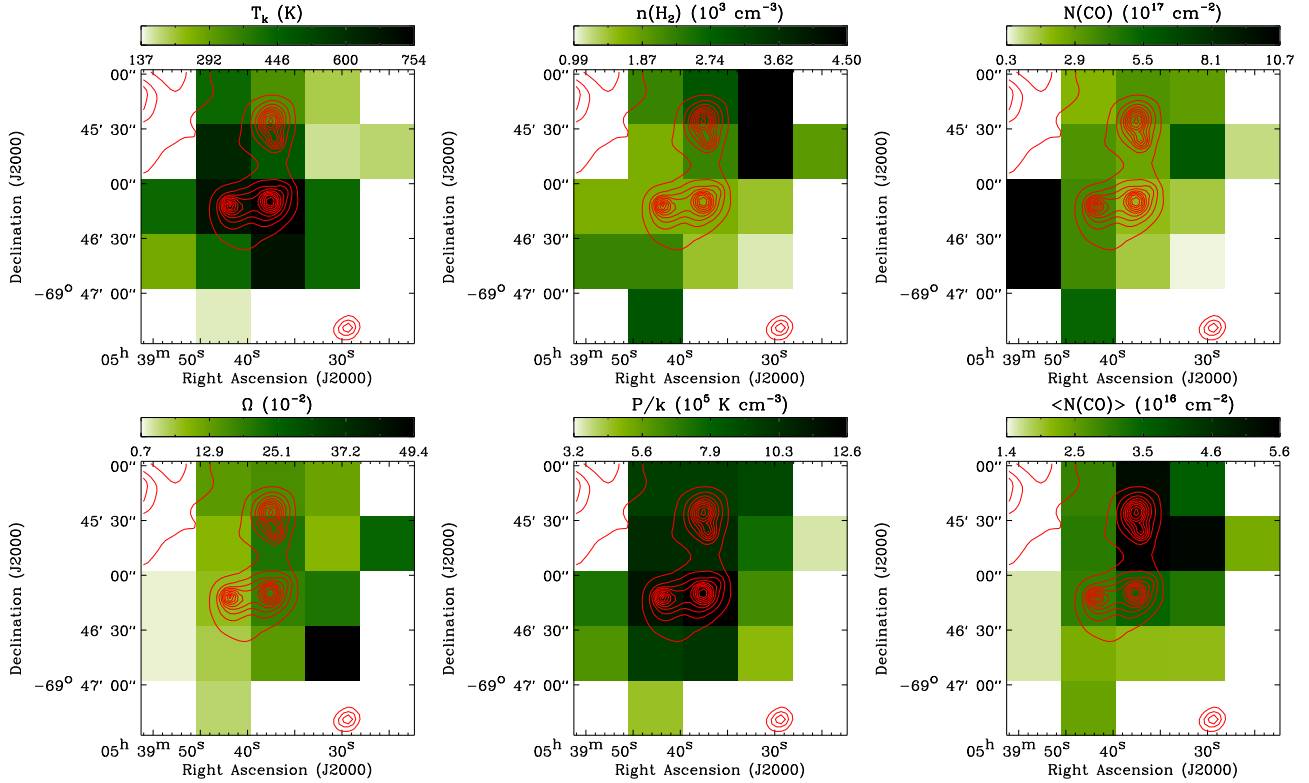


Fig. 11. Images of the RADEX best-fit parameters at 42'' resolution. The *Spitzer* 24 μm emission at its original resolution of 6'' is overlaid in red.

Table 2. Best-fit RADEX parameters and their uncertainties determined for the observed CO SLEDs.

Parameter	Minimum		Maximum		Median	
	All	Sub	All	Sub	All	Sub
T_k (K) ^a	153 ⁺⁷⁸ ₋₅₁	49 ⁺⁷⁶ ₋₃₀	754 ⁺¹³² ₋₁₁₂	569 ⁺⁴³¹ ₋₃₃₁	429 ⁺¹¹⁵ ₋₉₁	153 ⁺¹¹³ ₋₆₅
$n(\text{H}_2)$ (10^3 cm^{-3}) ^a	1.1 ^{+1.2} _{-0.6}	1.9 ^{+2.8} _{-1.2}	4.5 ^{+1.8} _{-1.3}	32.4 ^{+89.7} _{-23.8}	2.2 ^{+0.7} _{-0.5}	4.5 ^{+13.7} _{-3.4}
$N(\text{CO})$ (10^{17} cm^{-2}) ^a	0.4 ^{+1.9} _{-0.3}	0.9 ^{+4.7} _{-0.8}	10.7 ^{+36.4} _{-8.3}	13.5 ^{+56.6} _{-10.9}	3.4 ^{+1.5} _{-1.0}	7.6 ^{+36.8} _{-6.3}
Ω (10^{-1}) ^a	0.2 ^{+0.1} _{-0.1}	0.2 ^{+0.1} _{-0.1}	4.9 ^{+6.4} _{-2.8}	2.4 ^{+3.2} _{-1.4}	1.4 ^{+1.1} _{-0.6}	0.9 ^{+0.6} _{-0.4}
P/k (10^5 K cm^{-3}) ^b	3.6 ^{+6.1} _{-2.2}	3.6 ^{+6.1} _{-2.2}	12.6 ^{+2.3} _{-1.9}	16.0 ^{+40.6} _{-11.5}	9.5 ^{+1.7} _{-1.5}	8.7 ^{+19.2} _{-6.0}
$\langle N(\text{CO}) \rangle$ (10^{16} cm^{-2}) ^b	1.6 ^{+3.7} _{-1.1}	2.0 ^{+7.5} _{-1.6}	5.6 ^{+1.1} _{-0.9}	8.9 ^{+4.0} _{-2.7}	3.0 ^{+0.6} _{-0.5}	4.0 ^{+1.6} _{-1.1}

Notes. “All”: RADEX solutions determined using all available CO transitions (Sect. 4.2). “Sub”: RADEX solutions for CO transitions only up to $J = 7-6$ (Sect. 4.5). ^(a) Primary parameters. ^(b) Secondary parameters.

extra components in our RADEX modeling, since it would then introduce additional uncertainties, e.g., how different components are mixed and contribute to each CO transition. One component fitting has been done for both Galactic (e.g., Köhler et al. 2014) and extragalactic (e.g., Meijerink et al. 2013; Wu et al. 2015b) sources, while multiple components (up to three) have been used only in those cases where a single component clearly fails to reproduce the full CO SLEDs (e.g., Rangwala et al. 2011; Kamenetzky et al. 2012, 2014; Pellegrini et al. 2013; Israel et al. 2014; Papadopoulos et al. 2014; Rosenberg et al. 2014; Stock et al. 2015). In Sect. 5.4, however, we discuss the possible presence of a second component in the context of the origin of the CO emission.

4.4. Other general properties

In this section, we discuss several of the general properties deduced from RADEX modeling. First of all, the average H_2 densities of $\sim 2.2 \times 10^3 \text{ cm}^{-3}$ are much lower than the critical densities

of $\sim 10^4-10^6 \text{ cm}^{-3}$ (Table 1; Yang et al. 2010), suggesting that the FTS CO lines are sub-thermalized in N159W. In the optically thin case, their intensities depend on the kinetic temperature and density squared. For optically thick lines, the CO column density mainly determines the intensity. In our RADEX modeling, CO lines with $J_u = 3, 4, 5,$ and 6 are generally optically thick with $1 \lesssim \tau(\text{CO}) \lesssim 10$.

In addition, we find that the CO and dust temperatures have generally similar distributions (Spearman’s rank correlation coefficient of 0.8): both peak at around the main star-forming regions, (RA, Dec) $\sim (05^{\text{h}}39^{\text{m}}40^{\text{s}}, -69^{\circ}46'10'')$, and decrease toward the edge of our FTS coverage. An absolute comparison, however, shows that the dust temperature is always lower than the CO temperature with a narrower range of $T_{\text{dust}} \sim 25-33 \text{ K}$. In the ISM, gas and dust are not in thermodynamical equilibrium, except for very dense regions ($n(\text{H}_2) \gtrsim 10^6 \text{ cm}^{-3}$) where the gas and dust temperatures become comparable due to the strong gas-dust coupling (e.g., Goldsmith 2001). The relatively uniform dust temperature results in a wide range of $T_k/T_{\text{dust}} \sim 6-24$. On

Table 3. Comparison with previous CO excitation analyses.

Parameter	Location ^a	This work		Nikolić+07 ^d	Pineda+08 ^e	Mizuno+10 ^f
		All ^b	Sub ^c			
T_k (K)	[0, 2]	324^{+45}_{-40}	72^{+112}_{-44}	15–95	~80	~70
	[0, 1]	471^{+59}_{-53}	126^{+199}_{-77}			
$n(\text{H}_2)$ (10^3 cm^{-3})	[0, 2]	$2.9^{+0.8}_{-0.6}$	$16.0^{+32.2}_{-10.7}$	10	~10	~4
	[0, 1]	$2.2^{+0.5}_{-0.4}$	$7.9^{+16.1}_{-5.3}$			
$N(\text{CO})$ (10^{17} cm^{-2})	[0, 2]	$3.4^{+1.3}_{-0.9}$	$8.5^{+7.4}_{-4.0}$	6–12	~10 ^g	~35
	[0, 1]	$2.7^{+1.2}_{-0.8}$	$8.5^{+6.9}_{-3.8}$			
Ω (10^{-1})	[0, 2]	$1.6^{+0.4}_{-0.3}$	$1.0^{+0.4}_{-0.3}$	0.9–7.0	~2	
	[0, 1]	$2.1^{+0.6}_{-0.5}$	$1.0^{+0.4}_{-0.3}$			

Notes. ^(a) Pixel location (Fig. 8). [0, 2] and [0, 1] correspond to (05^h39^m36.8^s, -69°45′12.6″) and (05^h39^m36.8^s, -69°45′42.6″). ^(b) “All”: RADEX solutions determined using all available CO transitions (Sect. 4.2). ^(c) “Sub”: RADEX solutions for CO transitions only up to $J = 7-6$ (Sect. 4.5). ^(d) CO(1–0), CO(2–1), CO(3–2), ¹³CO(1–0), and ¹³CO(2–1) lines were modeled with the non-LTE radiative transfer model by Jansen et al. (1994). ^(e) CO ($J_u = 1, 4$, and 7), ¹³CO ($J_u = 1$ and 4), and [CI] (609 μm and 370 μm) transitions were analyzed using the escape probability radiative transfer model by Stutzki & Winnewisser (1985). ^(f) CO ($J_u = 1, 2, 3, 4$, and 7) and ¹³CO ($J_u = 1, 2, 3$, and 4) data were combined with the large velocity gradient (LVG) model by Goldreich & Kwan (1974). ^(d,e,f) All analyses were done on 45″ scales. ^(g) CO linewidth of 10 km s⁻¹ is used for this estimate.

average, the CO-to-dust temperature ratio is high with ~ 14 being the median value and this is reflected in the unusually high $L_{\text{CO}}/L_{\text{TIR}}$ of $\sim 8 \times 10^{-4}$ for N159W, which could hint at shock excitation (Sect. 5.3.4 for details).

Finally, we note that the CO-emitting gas in N159W is almost isobaric with the thermal pressure of $\sim 9.5 \times 10^5 \text{ K cm}^{-3}$, which seems high enough to be critical for the dynamics of HII regions. Recently, Lopez et al. (2014) measured several types of pressures exerted on the shells of 32 HII regions in the Magellanic Clouds (N159W not included) by analyzing radio, IR, optical, UV, and X-ray observations. These pressures were associated with direct stellar radiation, dust-processed IR radiation, warm ionized gas, and hot X-ray gas and the authors found that the warm ionized gas generally dominates over the other terms with the thermal pressure of $\sim (1-10) \times 10^6 \text{ K cm}^{-3}$. The pressure of the CO-emitting gas in N159W is indeed comparable with the warm ionized gas pressure, suggesting that the energy and momentum associated with the warm CO could also play a significant role in the evolution of HII regions.

4.5. Comparison with previous studies

A number of authors have also studied the physical conditions of the CO-emitting gas in N159W (e.g., Bolatto et al. 2005; Nikolić et al. 2007; Pineda et al. 2008; Minamidani et al. 2008; Mizuno et al. 2010). In this section, we compare our results with three of the most recent high-resolution studies: Nikolić et al. (2007), Pineda et al. (2008), and Mizuno et al. (2010). These studies analyzed mainly CO (up to $J = 7-6$) and ¹³CO (up to $J = 4-3$) transitions using various radiative transfer models and their results on 45″ scales are presented in Table 3. To make a comparison, we list our RADEX results for the pixels that are the closest to the pointings analyzed in the previous studies (“All” in Table 3).

The comparison between our work and the previous studies shows a large difference, particularly in T_k and $N(\text{CO})$: we estimate a much higher T_k ($\sim 300-500 \text{ K}$ vs. $\lesssim 100 \text{ K}$) and a much lower $N(\text{CO})$ ($\sim 3 \times 10^{17} \text{ cm}^{-2}$ vs. $\sim (10-40) \times 10^{17} \text{ cm}^{-2}$). This large discrepancy most likely arises from the fact that high- J CO transitions are included in our study and we test this

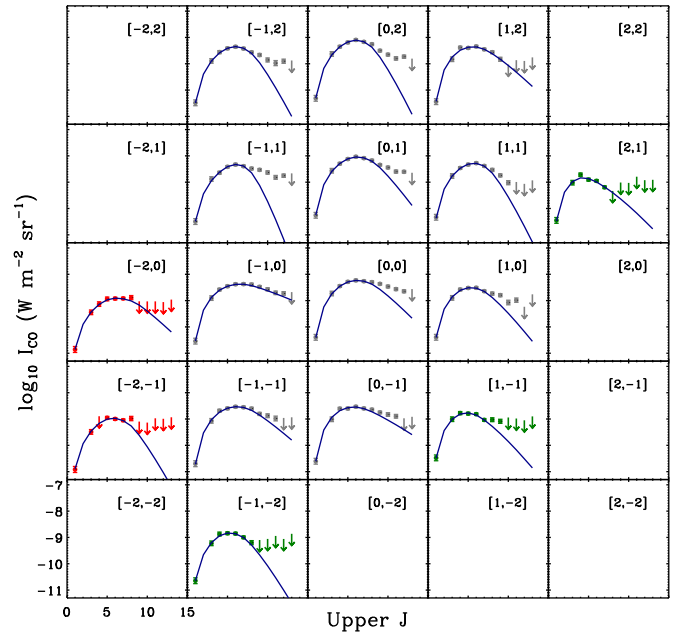


Fig. 12. RADEX best-fit curves (dark blue) obtained by modeling CO transitions only up to $J = 7-6$. The observed CO SLEDs in gray, red, and green are the same as in Fig. 8.

hypothesis by performing RADEX modeling following what we do in Sect. 4.2 but using CO lines only up to CO(7–6) (the highest transition in the previous studies). The best-fit models are shown in Fig. 12 and are summarized in Tables 2 and 3 (“Sub”).

As shown in Fig. 12, a single temperature component fits the CO SLEDs quite well up to $J = 7-6$ but deviates from $J = 8-7$. Excluding high- J CO transitions affects all RADEX parameters, particularly T_k , $n(\text{H}_2)$, and $N(\text{CO})$. The re-derived T_k is much lower than what we estimate in Sect. 4.2, while $n(\text{H}_2)$ and $N(\text{CO})$ increase in our re-modeling. The secondary parameters, P and $\langle N(\text{CO}) \rangle$, and the beam filling factor Ω are relatively less affected.

We find that the new parameters are indeed in reasonably good agreement with the results from the previous studies

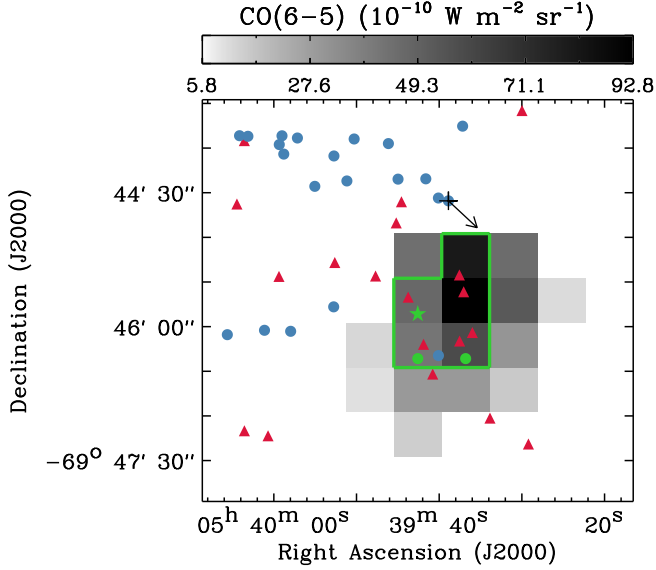


Fig. 13. UV and X-ray heating sources on the CO(6–5) integrated intensity image. Massive YSOs from [Chen et al. \(2010\)](#) are shown as the red triangles, while spectroscopically identified early-type stars from [Fariña et al. \(2009\)](#) are overlaid as the blue circles. The black cross and arrow indicate LMC X-1 and the orientation of its jet ([Cooke et al. 2007](#)). Finally, the five pixels used for our PDR modeling are outlined in green. The pixel indicated with the green star is the one presented in [Figs. 14 and 15](#) and the two other pixels with the green circles are the regions where particularly large discrepancies with the PDR model are found (Sect. 5.1.2).

(Table 3). Limiting the number of CO transitions, however, substantially increases the uncertainties in RADEX modeling and our original and newly-derived parameters are in fact consistent within 1σ errors except for T_k . Even for T_k , only 3 out of the total 16 pixels show statistically significant differences. All these results suggest that including high- J lines (beyond the CO SLED peak transition) is critical to characterize the physical conditions of CO emission with better accuracy.

5. Heating sources in N159W

To understand the origin of the warm CO in N159W, we consider four primary heating sources: UV photons, X-rays, cosmic-rays, and mechanical heating.

5.1. UV photons and X-rays

As one of the active star-forming regions in the LMC, N159W harbors massive stars whose intense UV radiation fields have a significant impact on the chemical and thermal structures of the ISM. Figure 13 shows the locations of such UV sources (massive YSOs from [Chen et al. 2010](#) and OB stars from [Fariña et al. 2009](#)) on the integrated intensity image of CO(6–5), the transition where most of the observed CO SLEDs peak (Sect. 4.1). Other than UV photons, X-rays from the nearby LMC X-1, the most powerful X-ray source in the LMC (Sect. 1; black cross in Fig. 13), could be another important source of heating. To probe the impact of UV and X-ray photons on the CO emission in N159W, we perform PDR modeling using an updated version of the Meudon PDR code (version 1.6; [Le Petit et al. 2006](#)). The major updates relevant for the present study are the implementation of (1) X-ray physics and (2) photo-electric heating based on the prescription by [Weingartner & Draine \(2001\)](#)

and [Weingartner et al. \(2006\)](#) instead of [Bakes & Tielens \(1994\)](#). These updates will be presented in a forthcoming paper ([Godard et al.](#), in prep.). Finally, the formation rate of H_2 is modeled considering the Eley-Rideal and Langmuir-Hinshelwood mechanisms as described in [Le Bourlot et al. \(2012\)](#). For computing time reason, we do not use the most sophisticated model of H_2 formation that considers random fluctuations in the dust temperature ([Bron et al. 2014](#)).

5.1.1. Meudon PDR modeling

The Meudon PDR code is a one-dimensional plane-parallel PDR model with one- or two-sided illumination. The model computes the distributions of atomic and molecular species for a slab of gas and dust based on thermal and chemical balance. For details on the chemical and physical processes and numerical computations in the model, we refer the reader to [Le Petit et al. \(2006\)](#).

In our analysis, each of the data points is modeled as a single cloud with a constant thermal pressure P , irradiated by a radiation field G_{UV} on two sides. The radiation field has the spectral shape of the interstellar radiation field in the solar neighborhood ([Mathis et al. 1983](#)) and its intensity varies with the scaling factor G_{UV} . $G_{UV} = 1$ corresponds to the integrated energy density of 6.8×10^{-14} erg cm^{-3} for 5–13.6 eV. To consider a range of the physical conditions in N159W, a large parameter space of $P/k = (3\text{--}3000) \times 10^4$ K cm^{-3} and $G_{UV} = 10\text{--}10^5$ is examined. For two-sided illumination, the varied $G_{UV} = 10\text{--}10^5$ is incident on only one side, while the fixed $G_{UV} = 1$ is used for the other side. Other important model parameters include: metallicity Z , PAH-to-dust mass ratio f_{PAH} , V-band dust extinction A_V (as a measure of the cloud size), X-ray flux G_X , and cosmic-ray ionization rate ζ_{CR} . For N159W, $Z = 0.5 Z_\odot$ and $f_{PAH} = 2\%$ (constrained by dust SED modeling; Sect. 2.4) are adopted and a range of A_V values, 0.5, 1, 3, 5, and 10 mag, are tested. To evaluate the impact of X-rays from LMC X-1, two values of $G_X = 0$ and 10 are then explored ($G_X = 1$ corresponds to the integrated energy density of 5.3×10^{-14} erg cm^{-3} for 0.2–10 keV). The second value of $G_X = 10$ is chosen to be the maximum incident X-ray flux we expect for the case where there is no absorption between LMC X-1 and N159W. Consequently, the influence of X-rays is in reality most likely weaker than the $G_X = 10$ case. As for ζ_{CR} , the typical value of 3×10^{-16} s $^{-1}$ for the diffuse ISM (e.g., [Indriolo & McCall 2012](#)) is adopted for the model. Finally, line opacities and intensities are calculated assuming the Doppler broadening of $(v_{th}^2 + v_{turb}^2)^{1/2}$, where $v_{th} = (2kT_k/m)^{1/2}$ is the thermal linewidth (m = mass of the atomic/molecular species) and v_{turb} is the microturbulent linewidth (3.5 km s $^{-1}$ is adopted in our study).

Our approach for PDR modeling is first to constrain P and G_{UV} by comparing the observed line ratios of ([OI] 145 μm + [CII] 158 μm)/FIR luminosity, [OI] 145 μm /[CII] 158 μm , and [CII] 158 μm /[CI] 370 μm with model predictions and then to see if the constrained conditions reproduce the measured CO intensities. For our purpose, the PACS and dust data presented in Sects. 2.2 and 2.4 are combined with the ground-based and FTS CO observations. All data sets are smoothed to 42'' resolution and cast onto the common grid, resulting in five pixels to work with (outlined in green in Fig. 13). The five pixels correspond to the main star-forming regions of N159W and this small number of pixels available for our PDR analysis is primarily due to the limited coverage of the PACS images (e.g., Fig. 4). Finally, we note that the [OI] 63 μm line is not included in our analysis due to the likely effect of high optical depth. The observed ratio of [OI] 145 μm /[OI] 63 μm is ≥ 0.1 over all five pixels, possibly

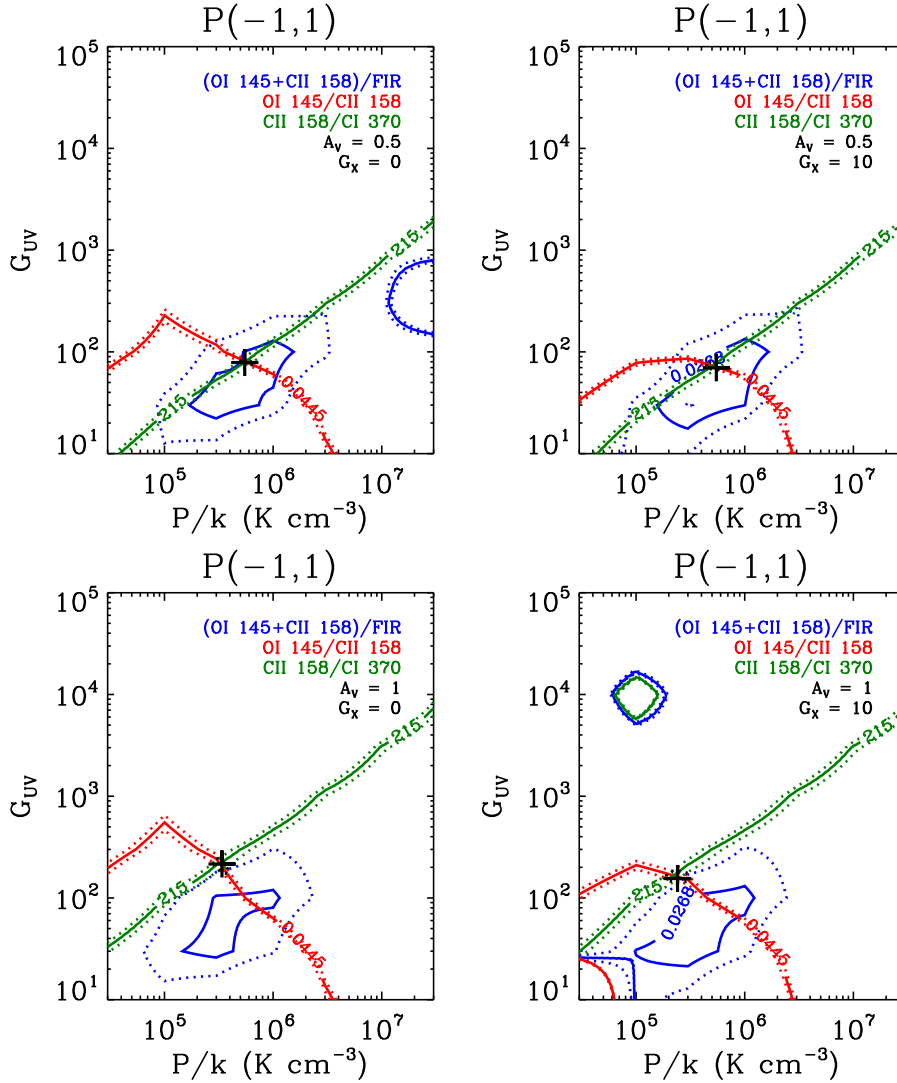


Fig. 14. Meudon PDR modeling of $([\text{OI}] 145 \mu\text{m} + [\text{CII}] 158 \mu\text{m})/\text{FIR}$ luminosity (blue), $[\text{OI}] 145 \mu\text{m}/[\text{CII}] 158 \mu\text{m}$ (red), and $[\text{CII}] 158 \mu\text{m}/[\text{CI}] 370 \mu\text{m}$ (green). This particular example is for the region at (RA, Dec) = $(05^{\text{h}}39^{\text{m}}43^{\text{s}}, -69^{\circ}45'43'')$, which corresponds to the pixel $[-1, 1]$ in Figs. 8 and 12. Each of the observed line ratios is shown as the solid line, while the 1σ uncertainty is in dotted line. The best-fit solution with the minimum χ^2 is indicated as the black cross. Finally, the following model parameters are used for each plot: $A_V = 0.5$ mag and $G_X = 0$ (top left), $A_V = 0.5$ mag and $G_X = 10$ (top right), $A_V = 1$ mag and $G_X = 0$ (bottom left), and $A_V = 1$ mag and $G_X = 10$ (bottom right). Note that the circular contours in the top left ($P/k > 10^7 \text{ K cm}^{-3}$ and $G_{\text{UV}} \sim 500$) and bottom right ($P/k \sim 10^5 \text{ K cm}^{-3}$ and $G_{\text{UV}} \sim 10^4$) plots are artifacts due to the unavailability of model predictions over the corresponding parameter ranges.

indicating that the $[\text{OI}] 63 \mu\text{m}$ transition is optically thick (e.g., Tielens & Hollenbach 1985).

5.1.2. Results

Our PDR modeling is done for all five pixels and we summarize overall findings in this section. The results for one pixel (shown with the green star in Fig. 13; $\sim 10 \text{ pc}$ size) are presented in Fig. 14 just as an illustration. First of all, we find that the observed three line ratios are well reproduced by the models with $A_V = 0.5$ mag. For the models with $A_V > 0.5$ mag, the $[\text{CII}] 158 \mu\text{m}/[\text{CI}] 370 \mu\text{m}$ ratio does not converge with the other two line ratios (this divergence becomes greater with increasing A_V), as shown in the bottom panels of Fig. 14 for $A_V = 1$ mag. The best-fit parameters (determined as having the minimum χ^2) for the PDR model with $A_V = 0.5$ mag and $G_X = 0$ are $P/k \sim (5-20) \times 10^5 \text{ K cm}^{-3}$ and $G_{\text{UV}} \sim 70-120$ across all five pixels. Other than P and G_{UV} , we can also constrain the beam filling

factor $\Omega \sim 5-7$ by comparing the observed $[\text{CII}] 158 \mu\text{m}$ intensity with the predicted value. Using other tracers (e.g., $[\text{OI}] 145 \mu\text{m}$ and $[\text{CI}] 370 \mu\text{m}$) results in essentially the same beam filling factors and $\Omega > 1$ suggests that multiple components exist along each line of sight. In fact, $\sim 5-7$ clouds whose individual A_V is ~ 0.5 mag are indeed in agreement with what we measure from dust SED modeling, $A_V \sim 2-3$ mag (probing the total dust abundance along the whole line of sight; Sect. 2.4). Finally, we find that the best-fit parameters for the models with $G_X = 0$ and $G_X = 10$ are comparable, implying that X-rays from the nearby LMC X-1 do not make a significant impact on the PDR tracers used in our analysis.

Now we investigate whether the constrained PDR conditions reproduce the ground-based and FTS CO observations. First, we compare the best-fit PDR solutions with our RADEX modeling results (Sect. 4.2) and find that the beam filling factor of the PDR tracers is a factor of ~ 40 larger than that of the CO lines, while the constrained pressure is in agreement. This

large difference in the beam filling factor could indicate that most of the CO emission in N159W does not originate from PDRs, where UV photons determine the thermal and chemical structures of the ISM. In addition, the kinetic temperature of ~ 70 K for the CO-emitting gas in the PDR model is lower than what we estimate for the CO lines via RADEX modeling (~ 320 – 750 K for the five pixels in our PDR analysis). The lower kinetic temperature has a substantial influence on CO emission and we indeed find that the predicted CO SLEDs are much fainter than the observed ones, as clearly shown in the top panels of Fig. 15. The discrepancy in the CO integrated intensity becomes greater with increasing J , e.g., from a factor of ~ 540 – 950 for CO(1–0) to a factor of $\sim (2.9$ – $8.3) \times 10^4$ for CO(12–11) ($A_V = 0.5$ mag and $G_X = 0$ case), and is particularly significant for the three pixels around the CO(6–5) peak (marked with the green star and circles in Fig. 13). In terms of the total CO integrated intensity (CO transitions from $J = 1$ –0 to $J = 12$ –11 are summed; $J = 2$ –1 excluded), the PDR model underestimates by a factor of a few $\times (10^2$ – $10^3)$. The shape of the observed CO SLEDs is also not reproduced by the PDR model. For example, the predicted CO SLEDs peak at either $J = 4$ –3 or $J = 5$ –4, while most of the observed CO SLEDs have a peak at $J = 6$ –5 (e.g., Fig. 8). In addition, the predicted CO SLEDs decrease beyond the peaks more steeply than what we measure in N159W, e.g., the ratio of CO(12–11) to CO(6–5) is ~ 0.2 – 0.4 in the observations, while $\sim (0.5$ – $1.2) \times 10^{-2}$ in the PDR model ($A_V = 0.5$ mag and $G_X = 0$ case). The failure of the PDR model to reproduce the shape of the observed CO SLEDs is also clearly shown in the middle panels of Fig. 15, where the three CO line ratios, CO(3–2)/CO(1–0), CO(6–5)/CO(3–2), and CO(9–8)/CO(6–5), do not converge to one solution over all parameter space. While the discrepancy we described so far is for the PDR model with $A_V = 0.5$ mag and $G_X = 0$, the presence of X-rays only slightly reduces the discrepancy (by only a factor of ~ 2 – 5 in the case of the total CO integrated intensity). Finally, we note that the PDR models with higher A_V values (up to 10 mag) still do not reproduce the observed CO(3–2)/CO(1–0), CO(6–5)/CO(3–2), and CO(9–8)/CO(6–5) ratios. To illustrate this result, PDR modeling with $A_V = 3$ mag is presented in the bottom panels of Fig. 15. Essentially, as A_V increases, the three CO line ratios go upward in the G_{UV} vs. P plot, but never converge to one solution.

In summary, our modeling of the [OI] $145 \mu\text{m}$, [CII] $158 \mu\text{m}$, [CI] $370 \mu\text{m}$, and FIR data suggests that the PDR component in the main star-forming regions of N159W has the thermal pressure $P/k \sim 10^6$ K cm^{-3} and the incident UV radiation field $G_{UV} \sim 100$. The CO emission originating from this PDR component is very weak and X-rays make only a minor difference. The majority of the observed CO emission (at least over the ~ 264 pc² region in our PDR analysis), therefore, must be excited by something other than UV photons and X-rays.

5.2. Cosmic-rays

Low-energy cosmic-rays ($E \sim 1$ – 10 MeV) are another important source of heating in the ISM. Cosmic-rays ionize atoms and molecules in collision and the substantial kinetic energy of the resulting primary electrons goes into gas heating (~ 35 eV and ~ 6 eV for the ionized and neutral medium respectively) through secondary ionization or excitation of atoms and molecules (e.g., Grenier et al. 2015). To evaluate the impact of cosmic-rays on the FIR fine-structure and CO lines, we examine one Meudon PDR model with an increased cosmic-ray ionization rate of $\zeta_{CR} = 3 \times 10^{-15} \text{ s}^{-1}$, which is ten times higher than the typical

value we use in Sect. 5.1.1. This particular PDR model has $A_V = 0.5$ mag, $P/k = 10^6$ K cm^{-3} , $G_{UV} = 10^2$, and $G_X = 10$, the model parameters that well reproduce the observed FIR line ratios. Note that there is only a negligible difference between the PDR models with $G_X = 0$ and 10. Our examination then reveals that the increased ζ_{CR} barely affects the FIR fine-structure and CO lines. To be specific, the [OI] $145 \mu\text{m}$, [CII] $158 \mu\text{m}$, and [CI] $370 \mu\text{m}$ lines change by $\sim 4\%$ at most, while the CO lines (up to $J = 13$ –12) vary by a factor of two.

Our exercise with the Meudon PDR model suggests that ζ_{CR} should be much higher than $3 \times 10^{-15} \text{ s}^{-1}$ to explain the discrepancy between the PDR model and the CO observations (Sect. 5.1.2). To quantify the cosmic-ray ionization rate that is required to fully reconcile the discrepancy, we then probe thermal balance in the regions analyzed with the PDR model as follows.

For the molecular ISM with the warm temperature of ~ 150 – 750 K and the intermediate density of a few $\times 10^3 \text{ cm}^{-3}$ (Table 2), H₂ is one of the primary coolants (e.g., Neufeld et al. 1995; Kaufman & Neufeld 1996). Based on the calculation of H₂ cooling function by Le Bourlot et al. (1999), we find the H₂ cooling rate of $\sim 10^{-23}$ – 10^{-22} erg s^{−1} per molecule. For this estimate, we use the RADEX-based kinetic temperature and ortho-to-para ratio (Sect. 4.2) and consider two atomic-to-molecular hydrogen ratios, $n(\text{H}^0)/n(\text{H}_2) = 10^{-2}$ and 1, the values suggested by Le Bourlot et al. (1999) for shocked-outflow and PDR conditions.

On the other hand, heating by cosmic-rays can be estimated as (e.g., Wolfire et al. 1995)

$$\Gamma_{CR} = \zeta_{CR} E_h n \text{ erg s}^{-1} \text{ cm}^{-3}, \quad (2)$$

where E_h = energy deposited as heat by a primary electron and $n = n(\text{H}^0) + 2n(\text{H}_2)$. To derive the cosmic-ray heating rate, we use $E_h = 6$ eV (appropriate for the neutral medium) and the RADEX-based H₂ density (Sect. 4.2). In addition, we explore two values of $n(\text{H}^0)/n(\text{H}_2) = 10^{-2}$ and 1, following our estimation of the cooling rate.

By equating the heating and cooling rates, we are then able to calculate $\zeta_{CR} \gtrsim 3 \times 10^{-13} \text{ s}^{-1}$, the cosmic-ray ionization rate that would fully account for the heating of the warm molecular medium in N159W. This estimate is a factor of $\gtrsim 1000$ higher than the typical value for the diffuse ISM. Recent *Fermi* observations of the LMC showed that the γ -ray emissivity in the N159W region is roughly 10^{-26} photons s^{−1} sr^{−1} per hydrogen atom at most (Abdo et al. 2010), which is comparable to the value measured for the local diffuse ISM in the Milky Way (Abdo et al. 2009). The cosmic-ray density in N159W is hence most likely not too different from the diffuse ISM value, ruling out cosmic-rays as the main energy source for the warm CO in the regions analyzed with the Meudon PDR model.

5.3. Mechanical heating

Along with UV photons, X-rays, and cosmic-rays, which primarily arise from the microscopic processes in the ISM, the macroscopic motions of gas can be an important source of heating. For example, energetic events such as stellar explosions (novae and supernovae), stellar winds, expanding HII regions, and converging flows strongly perturb the surrounding ISM and drive shocks. The shocks then accelerate, compress, and heat the medium, effectively converting much of the injected mechanical energy into thermal energy.

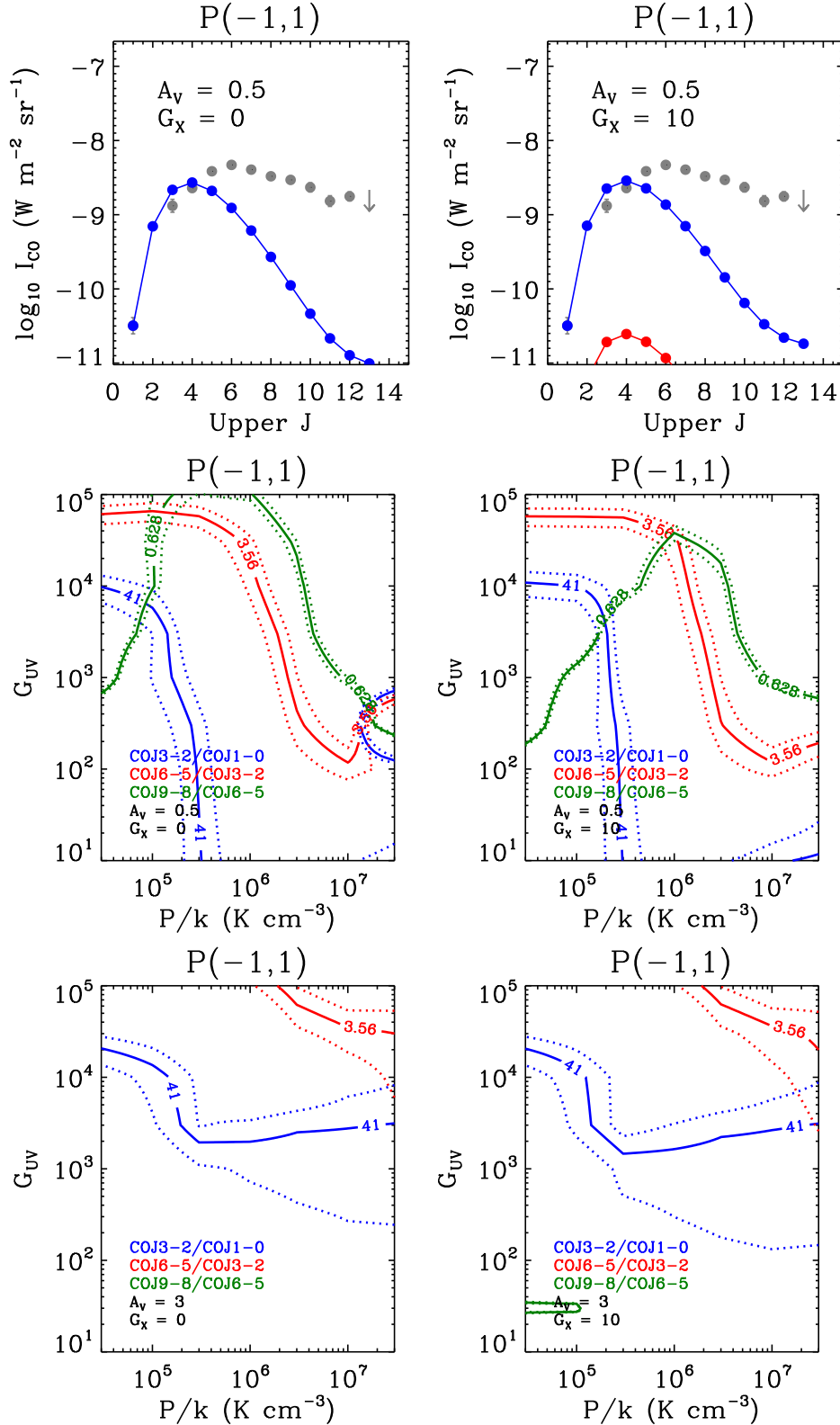


Fig. 15. Meudon PDR modeling of CO lines. As in Fig. 14, all plots presented here are for the region at (RA, Dec) = (05^h39^m43^s, -69°45'43'') ([-1, 1] in Figs. 8 and 12). The *left and right panels* are for $G_X = 0$ and $G_X = 10$ respectively. *Top:* CO SLEDs: observations (gray) vs. model predictions (red). The CO predictions are from the best-fit solutions in the top panels of Fig. 14 and are too low to be shown for $G_X = 0$. For an easy comparison with the observed SLEDs, the model SLEDs are also scaled to match the CO(1-0) integrated intensities and are presented in blue. *Middle:* model results for the line ratios ($A_V = 0.5$ mag): CO(3-2)/CO(1-0) (blue), CO(6-5)/CO(3-2) (red), and CO(9-8)/CO(6-5) (green). Each of the observed line ratios is shown as the solid line, while the 1σ uncertainty is the dotted line. Note that the circular contours in the *middle left plot* at $P/k > 10^7 \text{ K cm}^{-3}$ and $G_{\text{UV}} \sim 500$ are artifacts due to the unavailability of model predictions over the corresponding parameter space. *Bottom:* same as the middle panels, but with $A_V = 3$ mag. Likewise, the ellipsoidal contour in the *bottom right plot* at $P/k < 10^5 \text{ K cm}^{-3}$ and $G_{\text{UV}} \sim 30$ is simply an artifact. Note that the observed CO(9-8)/CO(6-5) ratio is not reproduced over the entire parameter space.

5.3.1. Paris-Durham shock modeling

In this section, we evaluate the impact of mechanical heating in N159W by comparing the observed CO and fine-structure lines with predictions from the Paris-Durham shock code (Flower & Pineau des Forêts 2015). This code simulates one-dimensional stationary J- or C-type shocks and calculates the dynamical and chemical properties of a multi-fluid medium (neutrals and ions), including densities, temperatures, velocities, and chemical abundances. For our study, we use the modified version by Lesaffre et al. (2013), which enables us to model UV-irradiated shocks, and create a grid of models covering the following input parameters: pre-shock density $n_{\text{pre}} = 10^4$, 10^5 , and 10^6 cm^{-3} , magnetic field parameter $b = 1$ (defined as $(B/\mu\text{G})/(n_{\text{pre}}/\text{cm}^{-3})^{1/2}$, where B is the strength of the magnetic field transverse to the direction of shock propagation), metallicity $Z = 1 Z_{\odot}$, UV radiation field $G'_{\text{UV}} = 0$ and 1 (defined as a scaling factor with respect to the interstellar radiation field by Draine 1978), and shock velocity v_s from 4 km s^{-1} to 20 km s^{-1} with 2 km s^{-1} steps. Given the input densities and magnetic field parameter, our model grid only contains stationary C-type shocks (e.g., Le Bourlot et al. 2002; Flower & Pineau des Forêts 2003). To compare with the observed CO SLEDs, we then employ a post-processing treatment based on the LVG approximation, following the method used in Gusdorf et al. (2012), Anderl et al. (2014), and Gusdorf et al. (2015). In our modeling, the effects of grain-grain interactions (e.g., Guillet et al. 2011; Anderl et al. 2013) are not considered, since these effects play an important role only for high density and shock velocity ($n_{\text{pre}} > 10^4 \text{ cm}^{-3}$ and $v_s > 20 \text{ km s}^{-1}$) cases. Finally, we note that reducing the input metallicity by a factor of two to match the LMC value ($\sim 0.5 Z_{\odot}$; e.g., Pagel 2003) would not change our main results. While the impact of low metallicity on the propagation of shocks has not been comprehensively examined, our preliminary analysis suggests that the CO and fine-structure line intensities would be affected by less than a factor of two in a half solar metallicity environment (Appendix B). Shock models with $Z < 1 Z_{\odot}$ are currently under development and we hence focus on solar metallicity models in this study.

5.3.2. Results: CO and fine-structure lines

A subset of the Paris-Durham shock models is presented in Fig. 16 with the observed CO SLEDs. To take into account the effect of beam dilution, the RADEX-based beam filling factor Ω is applied to the predicted intensities on a pixel-by-pixel basis. We find that the shock models with $n_{\text{pre}} = 10^4 \text{ cm}^{-3}$, $G'_{\text{UV}} = 0$, and $v_s \sim 6\text{--}14 \text{ km s}^{-1}$ reproduce our observations relatively well. In these models, gas is initially shocked with Mach and Alfvénic Mach numbers of ~ 40 and ~ 5 . For the CO-bright layers ($A_V \sim 2 \text{ mag}$), the temperatures reach up to $\sim 180 \text{ K}$ and $\sim 800 \text{ K}$ for $v_s = 6 \text{ km s}^{-1}$ and 14 km s^{-1} respectively and the post-shock densities are intermediate with a few $\times 10^4 \text{ cm}^{-3}$, which are in reasonably good agreement with our RADEX-based estimates (Sect. 4.2). On the other hand, the same shock models significantly underestimate the [CII] $158 \mu\text{m}$, [OI] $63 \mu\text{m}$, and [OI] $145 \mu\text{m}$ intensities by up to a factor of a few $\times 10^6$ for [CII] $158 \mu\text{m}$ and a factor of a few $\times 10^2$ for [OI] $63 \mu\text{m}$ and $145 \mu\text{m}$. Note that this discrepancy persists even if we make an extreme assumption of $\Omega = 1$, e.g., the fine-structure lines entirely fill the $42''$ beam. While the current analyses have several limitations (e.g., only a single shock is considered over a small parameter space and the model parameters are degenerate), our results clearly demonstrate that mechanical heating by shocks

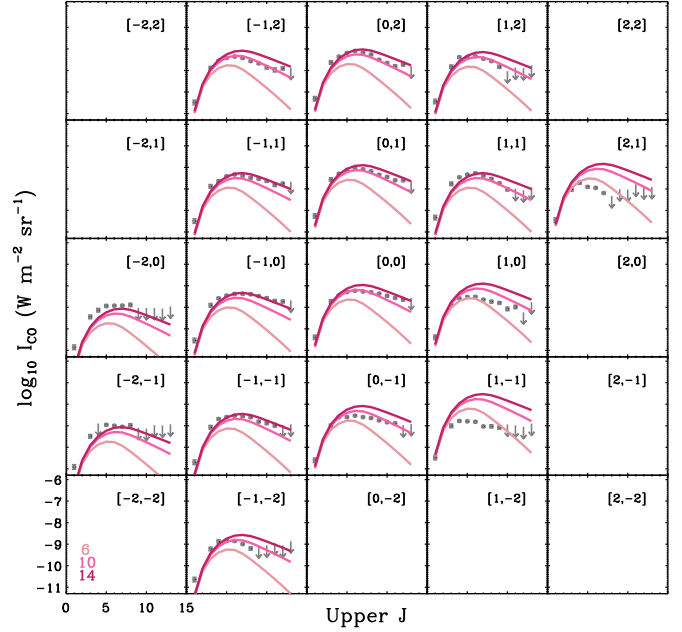


Fig. 16. Comparison between the observed CO SLEDs (gray) and the Paris-Durham shock models with $n_{\text{pre}} = 10^4 \text{ cm}^{-3}$, $G'_{\text{UV}} = 0$, and $v_s = 6$, 10, and 14 km s^{-1} (pink). The different shock velocities are also indicated in the bottom left corner of the plot.

can reproduce the observed CO intensities. The shock contributions to the [CII] $158 \mu\text{m}$, [OI] $63 \mu\text{m}$, and $145 \mu\text{m}$ transitions are small, however, and these fine-structure lines are therefore most likely heated by other sources, e.g., UV photons. This conclusion is consistent with our PDR modeling (Sect. 5.1.2), where the observed fine-structure line ratios are well reproduced by a single PDR component with $P/k \sim 10^6 \text{ K cm}^{-3}$ and $G_{\text{UV}} \sim 100$.

5.3.3. Results: energetics

We now study the shock energetics in N159W. Our method follows the procedure presented in Anderl et al. (2014) and Gusdorf et al. (2015), but for the shock parameters that reproduce our CO observations: $n_{\text{pre}} = 10^4 \text{ cm}^{-3}$, $b = 1$, $Z = 1 Z_{\odot}$, $G'_{\text{UV}} = 0$, and $v_s \sim 6\text{--}14 \text{ km s}^{-1}$. In essence, the Paris-Durham shock code predicts the fluxes of mass, momentum, and energy and we derive the total mass, momentum, and energy per modeled position in N159W by adopting a reasonable estimate for the size of shocked regions. To be specific, we assume a cylindrical shape for the shocked regions along each line of sight and use a circle with a diameter of $30''$ (FTS pixel size; corresponding to $\sim 41.5 \text{ pc}^2$ at the LMC distance) for the surface area. As for the line of sight depth, we choose it as the length a neutral particle travels for 10^5 yr with a shock velocity of v_s (e.g., $\sim 0.2 \text{ pc}$ for the model with $v_s = 10 \text{ km s}^{-1}$). This timescale of 10^5 yr is the typical time needed for the shocked gas to return to equilibrium after the passage of a shock wave with the characteristics considered in our analysis, as well as a satisfactory upper limit on the age of shocks associated with star formation or supernova remnants (e.g., Wolszczan et al. 1991; Williams et al. 2006; André 2011). Finally, we use the RADEX-based beam filling factor of $\Omega = 0.1$ to scale the predicted energetics, a representative value for the shocked CO clumps in the FTS pixels (Table 2). Bearing the uncertainties in our calculations (e.g., the stationary and one-dimensional model and the simplified cylindrical geometry with the less-known timescale for shocks), we find the total mass of

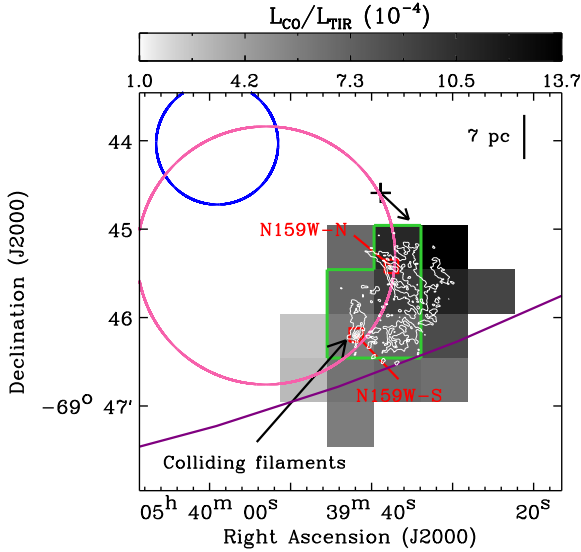


Fig. 17. Possible shock drivers overlaid on the $L_{\text{CO}}/L_{\text{TIR}}$ image (Sect. 5.3.4 for details). (1) LMC X-1 and its proposed jet (black cross and arrow; the angle of the jet was estimated by [Cooke et al. 2007](#)); (2) SNR J0540.0–6944 (blue circle; the diameter corresponds to the size of ~ 19 pc measured by [Williams et al. 2000](#)); (3) protostellar outflows (red squares; N159W-N and N159W-S); (4) colliding filaments; (5) SGS 19 (purple circle; this HI supergiant shell cataloged by [Kim et al. 1999](#) is only partially shown here); and (6) wind-blown bubble (pink circle; the diameter is ~ 40 pc, as suggested by [Jones et al. 2005](#)). The ALMA CO(2–1) observations on $\sim 1''$ scales where the protostellar outflows and the colliding filaments were identified ([Fukui et al. 2015](#)) are shown as the white contours with levels ranging from 10% to 90% of the peak (29 Jy Beam^{-1}) in 20% steps. The five pixels used in our Meudon PDR modeling (Sect. 5.1.1) are also outlined in green.

shocked gas per modeled position of $\sim (0.9\text{--}2) \times 10^3 M_{\odot}$, which is roughly the mass of small molecular clouds or a small fraction ($\sim 1\text{--}10\%$) of the mass of typical molecular clouds in the Milky Way (e.g., [Dobbs et al. 2014](#)). The total momentum injected by shocks on each modeled position is of the order of $(0.6\text{--}3) \times 10^4 M_{\odot} \text{ km s}^{-1}$, which is $\sim 10^5$ and $\sim 10^3$ times higher than that found for the shocks associated with the BHR71 low-mass stellar outflow ([Gusdorf et al. 2015](#)) and the relatively old supernova remnant W44 ([Anderl et al. 2014](#)) respectively. This large difference in the total momentum mainly results from the fact that the mass of shocked gas is much higher in N159W. Finally, the total energy dissipated by shocks is $\sim (0.4\text{--}4) \times 10^{48}$ erg, which can for instance be compared with the typical 10^{51} erg released by one supernova explosion (e.g., [Hartmann 1999](#)). In our calculations, one of the most uncertain parameters is the timescale of shocks, which can be off from the current value of 10^5 yr by an order of magnitude. Our energetics estimates would then need to be scaled accordingly.

5.3.4. Origin of shocks

The reasonably good agreement with the Paris-Durham model suggests that shocks are most likely the dominant heating source for the warm CO in N159W. Then what can drive these shocks? There are a few candidates (Fig. 17) and we discuss them here.

1. LMC X-1: [Cooke et al. \(2007\)](#) observed the filamentary nebula surrounding LMC X-1 (N159F; [Henize 1956](#)) in several optical lines ($\text{H}\alpha$, [OI], [NII], [SII], [ArIII], and HeI)

and found that all emission lines show a bow shock morphology. This shock structure was seen ~ 4 pc away from LMC X-1 and was attributed to a presently unobserved jet from LMC X-1 (black cross and arrow in Fig. 17). The observed line ratios were analyzed using the radiative shock model by [Hartigan et al. \(1987\)](#) and the jet-driven shock velocity of $\sim 90 \text{ km s}^{-1}$ was constrained.

2. SNR J0540.0–6944: [Williams et al. \(2000\)](#) examined the X-ray emission from SNR J0540.0–6944 (blue circle in Fig. 17) using *Chandra* observations and found that the SNR has a thick-shelled structure (~ 19 pc in diameter). The observed X-ray structure indicated that SNR J0540.0–6944 is undergoing Sedov-like expansion and the SNR-driven shock velocity of 240 km s^{-1} was estimated.
3. Protostellar outflows: [Fukui et al. \(2015\)](#) recently found two molecular outflows, N159W-N and N159W-S (red squares in Fig. 17), from their ALMA CO(2–1) observations at $\sim 1''$ resolution. This was the first discovery of extragalactic protostellar outflows. The outflows were found to have a velocity span of $10\text{--}20 \text{ km s}^{-1}$ and to be associated with two massive YSOs previously studied by [Chen et al. \(2010\)](#). Redshifted and blueshifted lobes were clearly found for N159W-S, while N159W-N shows a blueshifted lobe only. All observed lobes are less than 0.2 pc. We note, however, that the active star-forming region N159W likely contains more stellar outflows, which have not been resolved in previous observations due to a lack of proper spatial and spectral resolution.
4. Colliding filaments: interestingly, N159W-S was found at the intersection of two filamentary clouds. The two filaments have a width of 0.5–1 pc and a length of 5–10 pc and are clearly separated based on their blueshifted and redshifted velocities. [Fukui et al. \(2015\)](#) hypothesized that the two filaments collided ~ 0.1 Myr ago with a velocity of $\sim 8 \text{ km s}^{-1}$, triggering the formation of N159W-S. As recently demonstrated by [Wu et al. \(2015a, 2016\)](#) with magnetohydrodynamic simulations, cloud-cloud collisions can drive shocks into the ISM.
5. Large-scale bubbles: N159W appears to be associated with large-scale bubbles that are considered to be produced by stellar feedback. For example, [Jones et al. \(2005\)](#) proposed that several O-type stars formed at the center of N159 about 1–2 Myr ago, driving a bubble with a radius of ~ 20 pc (pink circle in Fig. 17). N159W is at the periphery of this wind-blown bubble. In addition, the systematic search of large HI structures in the LMC by [Kim et al. \(1999\)](#) showed that N159W is located along the western edge of SGS 19 (purple circle in Fig. 17). This HI supergiant shell centered at (RA, Dec) = $(05^{\text{h}}41^{\text{m}}27^{\text{s}}, -69^{\circ}22'23'')$ has a radius of ~ 380 pc and an expansion velocity of $\sim 25 \text{ km s}^{-1}$ ([Dawson et al. 2013](#)). Several other HI supergiant shells (SGSs 12, 13, 15, 16, 17, 20, and 22) were found surrounding SGS 19 (Fig. 1), which may indicate that SGS 19 formed by sequential star formation ([Kim et al. 1999](#)). The counterpart shell in $\text{H}\alpha$, LMC2 (brightest $\text{H}\alpha$ SGS in the LMC; [Book et al. 2008](#)), was also identified and seen to be confined to the inner edge of SGS 19.
6. Milky Way-Magellanic Clouds interaction: while the interaction between the Milky Way and the Magellanic Clouds and its impact on the evolution of gas and stars are currently under debate ([D’Onghia & Fox 2016](#)), it is most likely that the tidal force and/or ram pressure are at work in the southeastern HI overdensity region in the LMC, where N159W is located (Fig. 1). For example, this HI overdensity region corresponds to the leading edge toward the Milky Way

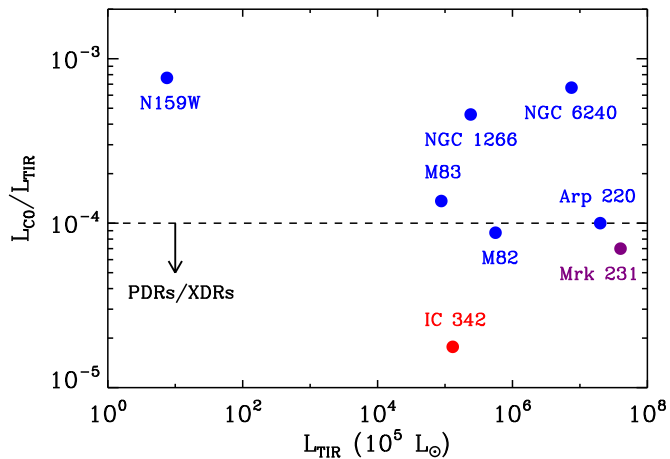


Fig. 18. $L_{\text{CO}}/L_{\text{TIR}}$ as a function of L_{TIR} for various extragalactic sources: NGC 6240 (Meijerink et al. 2013), NGC 1266 (Pellegrini et al. 2013), M83 (Wu et al. 2015b), Arp 220 (Rangwala et al. 2011), M82 (Kamenetzky et al. 2012), Mrk 231 (van der Werf et al. 2010), and IC 342 (Rigopoulou et al. 2013). The sources are color coded based on the dominant heating mechanism: UV photons (red), X-rays (purple), and mechanical heating (blue). In addition, the threshold of $L_{\text{CO}}/L_{\text{TIR}} \lesssim 10^{-4}$ proposed by Meijerink et al. (2013) for PDRs and XDRs is shown as the dashed line.

halo and de Boer et al. (1998) indeed suggested that a large amount of neutral gas was built up as a result of ram pressure of the hot halo gas on the LMC. In addition, the HI overdensity region appears to be connected with the Magellanic Bridge that exists between the LMC and the SMC (e.g., Kim et al. 1998; Putman et al. 2003), hinting at its tidal origin (e.g., Bekki & Chiba 2007; Besla et al. 2012).

We note that the good agreement with the Paris-Durham model is found for every pixel in Fig. 16, which implies that CO is shock-heated across the entire FTS coverage ($\sim 40 \text{ pc} \times 40 \text{ pc}$ region). This conclusion is also consistent with the fact that all individual pixels in our analysis have $L_{\text{CO}}/L_{\text{TIR}} \gtrsim 10^{-4}$. The threshold of $L_{\text{CO}}/L_{\text{TIR}} \gtrsim 10^{-4}$ is the diagnostic for shocks proposed by Meijerink et al. (2013) based on extensive theoretical modeling of UV and X-ray dominated regions (PDRs and XDRs; Meijerink & Spaans 2005; Meijerink et al. 2007). Essentially, Meijerink et al. (2013) argued that star-forming regions and active galactic nuclei creating PDRs and XDRs heat both gas and dust. On the other hand, shocks do not heat dust as effectively as they do for gas. As a result, CO line-to-TIR continuum ratios are expected to be higher in shocks than in PDRs and XDRs. The measured $L_{\text{CO}}/L_{\text{TIR}}$ is indeed $\sim 8 \times 10^{-4}$ for the entire N159W, which is comparable to that of other extragalactic sources where mechanical heating was found to be the dominant heating mechanism for CO (e.g., NGC 6240, NGC 1266, Arp 220, M82, and M83; Fig. 18). However, the regions of the largest discrepancy with the PDR model (shown as the green star and circles in Fig. 13) do not exactly correspond to the pixels with high $L_{\text{CO}}/L_{\text{TIR}}$ values: two other pixels with less discrepancy have higher $L_{\text{CO}}/L_{\text{TIR}}$. This indicates that the diagnostic power of the L_{CO} -to- L_{TIR} ratio needs further investigation.

In summary, while all the candidates we describe can trigger shocks, large-scale physical processes, e.g., powerful stellar winds and supernova explosions that created supergiant bubbles in the LMC and Milky-Way-Magellanic Clouds interactions, are likely the primary drivers of shocks that heat CO in N159W. To test this hypothesis and evaluate how pervasive shocks are in

the LMC, multiple CO transitions should be systematically examined over the entire LMC along with other tracers of PDRs and shocks (e.g., FIR fine-structure lines, SiO transitions, etc.). In particular, direct shock tracers such as SiO emission would be critical to constrain the properties of shocks with better accuracy, breaking the model degeneracy.

5.4. Synthesized view

In this section, we provide a synthesized view of the CO and fine-structure lines in N159W. In essence, our PDR and shock modeling indicate the presence of two distinct components: low- and high-extinction media where UV photons and shocks control the thermal and chemical structures of gas respectively. The low-extinction component fills the entire $42''$ beam with $A_V \sim 0.5$ mag and several clouds of this kind exist along a line of sight providing the total extinction of a few magnitudes. The medium is primarily heated by UV photons up to ~ 70 K and emits very weak CO emission as a consequence of the low temperature and the low CO abundance at $A_V \sim 0.5$ mag. On the other hand, [OI] $145 \mu\text{m}$, [CII] $158 \mu\text{m}$, and [CI] $370 \mu\text{m}$ are bright, explaining the fine-structure line observations of N159W. The second high-extinction component has a much smaller beam filling factor of ~ 0.1 and is shock-heated up to ~ 800 K. This warm medium has $A_V \sim 2$ mag on average and could be further shielded against dissociating UV photons by the first low-extinction component and other possible pre-shock medium (whose existence can be hinted by the excess of low- J CO emission for several pixels compared to the shock model predictions; e.g., $[-2, -1]$ and $[-2, 0]$ in Fig. 16). As a result, abundant CO molecules can form and survive, reproducing the CO observations of N159W. On the contrary, the [OI] $145 \mu\text{m}$, [CII] $158 \mu\text{m}$, and [CI] $370 \mu\text{m}$ fine-structure lines are weak. The two components are roughly in pressure equilibrium with $\sim 10^6 \text{ K cm}^{-3}$.

We note that this interpretation is also compatible with our RADEX modeling. While the two components exist in N159W, the low-extinction, relatively cold one produces little CO emission (mainly at $J_u \lesssim 4$). On the other hand, the high-extinction, shock-heated warm medium emits bright in CO. This picture is in agreement with Sect. 4.2, where we find that the observed CO SLEDs are well reproduced with a single warm component.

6. Conclusions

We present *Herschel* SPIRE FTS observations of N159W, one of the most active star-forming regions in the LMC. Along with other multiwavelength tracers of gas and dust, the FTS observations are analyzed to examine the physical properties and excitation conditions of molecular gas ($42''$ scales; corresponding to $\sim 10 \text{ pc}$). Our main results can be summarized as follows.

1. In our FTS observations, CO rotational lines with J_u (upper level J) = 4–12 and [CI] ($609 \mu\text{m}$ and $370 \mu\text{m}$) and [NII] ($205 \mu\text{m}$) fine-structure lines are detected across the star-forming region.
2. Intermediate- ($6 \leq J_u \leq 9$) and high- J ($J_u \geq 10$) CO lines show more compact spatial distributions than low- J ($J_u \leq 5$) CO lines. To be specific, the measured full width at half maximum is $42''$ – $60''$ for the low- J transitions, while $< 42''$ for the intermediate- and high- J transitions. The two [CI] transitions are as compact as the intermediate- J CO transitions.
3. Combined with ground-based CO(1–0) and CO(3–2) observations, the FTS CO data are used to construct CO SLEDs on a pixel-by-pixel basis. We find that the peak and slope of the

observed CO SLEDs change across the region, implying spatial variations in the physical conditions of the CO-emitting gas.

4. The observed CO SLEDs are modeled with the non-LTE radiative transfer code RADEX and the following parameters are constrained across N159W on ~ 10 pc scales: kinetic temperature $T_k = 153\text{--}754$ K, H_2 density $n(\text{H}_2) = (1.1\text{--}4.5) \times 10^3 \text{ cm}^{-3}$, CO column density $N(\text{CO}) = (0.4\text{--}10.7) \times 10^{17} \text{ cm}^{-2}$, beam filling factor $\Omega = 0.02\text{--}0.5$, thermal pressure $P/k = (3.6\text{--}12.6) \times 10^5 \text{ K cm}^{-3}$, and beam-averaged CO column density $\langle N(\text{CO}) \rangle = (1.6\text{--}5.6) \times 10^{16} \text{ cm}^{-2}$.
5. We find that excluding CO transitions with $J_u > 7$ affects all RADEX parameters, in particular T_k , $n(\text{H}_2)$, and $N(\text{CO})$ (T_k underestimated and $n(\text{H}_2)$ and $N(\text{CO})$ overestimated along with larger 1σ uncertainties, compared to the case where CO transitions up to $J = 12\text{--}11$ are modeled). This suggests that high- J lines (beyond the SLED peak transition) are crucial to quantify the physical properties of CO-traced molecular gas more accurately.
6. While constraining the properties of PDRs traced by [OI] $145 \mu\text{m}$, [CII] $158 \mu\text{m}$, [CI] $370 \mu\text{m}$, and far-infrared luminosity (dust extinction $A_V \sim 0.5$ mag, thermal pressure $P/k \sim 10^6 \text{ K cm}^{-3}$, and incident UV radiation field $G_{\text{UV}} \sim 100$ in the Mathis field units), the Meudon PDR model used in our analysis fails to explain the CO observations. Specifically, both the amplitude and slope of the observed CO SLEDs are not reproduced, suggesting that the CO-emitting gas in N159W must be excited by something other than UV photons.
7. X-rays from LMC X-1, the most strong X-ray source in the LMC, are found to have only a minor contribution to the CO emission. In addition, cosmic-rays are most likely not abundant enough to reproduce the observed warm CO, ruling out X-rays and cosmic-rays as the dominant heating source for CO in N159W.
8. While only a limited parameter space is searched, our shock modeling with the Paris-Durham code clearly demonstrates that shocks can produce enough energy to excite the warm CO in N159W. On the other hand, the same shocks are faint in [CII] $158 \mu\text{m}$, [OI] $63 \mu\text{m}$, and $145 \mu\text{m}$. Several sources are considered as possible shock drivers and large-scale processes involving powerful stellar winds and supernova explosions that carved supergiant shells in the LMC and Milky Way-Magellanic Clouds interactions are likely the primary energy source for CO.

Our study of N159W in the LMC adds further evidence that the warm molecular medium is pervasive and CO rotational transitions are powerful diagnostic tools to probe the physical conditions of the medium. CO lines alone, however, have proven to be insufficient to pin down the origin of this warm molecular component in the ISM and additional tracers have been found to be critical for the analysis. For example, our Meudon PDR modeling shows that FIR fine-structure lines are essential to evaluate the contribution of UV photons to CO heating. In addition, [Rosenberg et al. \(2014a,b\)](#) suggested that dense gas tracers such as HCN, HNC, and HCO^+ can be used to differentiate between UV-driven heating and mechanical heating. Molecular ions like H_2O^+ and OH^+ were found particularly valuable to examine X-ray/cosmic-ray-driven heating and chemistry (e.g., [van der Werf et al. 2010](#); [Spinoglio et al. 2012](#)).

Our work also supports the emerging picture that mechanical heating plays an important role in the excitation of molecular gas. In general, however, the source of mechanical heating has

not been well-constrained, mostly because previous studies have not had high enough angular and spectral resolutions to resolve the drivers of mechanical energy, e.g., stellar winds/outflows, supernova explosions, spiral waves, and galaxy interactions. Systematic studies of various atomic and molecular species at high spatial and spectral resolutions are crucial to probe the driver(s) of mechanical heating and the detailed processes of energy dissipation in the ISM (e.g., [Herrera et al. 2012](#); [Larson et al. 2015](#); [Rangwala et al. 2015](#)), which will be possible particularly with ALMA, NOEMA, and JWST.

Acknowledgements. We would like to thank the anonymous referee for the constructive comments that improved this work. We also thank Julia Kamenetzky, Edward Polehampton, Eric Pellegrini, and Naseem Rangwala for helpful discussions on FTS data reduction and science. M.-Y.L. acknowledges support from the DIM ACAV of the Region Ile de France, the SYMPATICO grant (ANR-11-BS56-0023) of the French Agence Nationale de la Recherche, and the CNRS PCMI program. S.H. acknowledges financial support from DFG programme HO 5475/2-1. PACS has been developed by a consortium of institutes led by MPE (Germany) and including UVIE (Austria); KU Leuven, CSL, IMEC (Belgium); CEA, LAM (France); MPIA (Germany); INAF-IFSI/OAA/OAP/OAT, LENS, SISSA (Italy); IAC (Spain). This development has been supported by the funding agencies BMVIT (Austria), ESA-PRODEX (Belgium), CEA/CNES (France), DLR (Germany), ASI/INAF (Italy), and CI-CYT/MCYT (Spain). SPIRE has been developed by a consortium of institutes led by Cardiff University (UK) and including Univ. Lethbridge (Canada); NAOC (China); CEA, LAM (France); IFSI, Univ. Padua (Italy); IAC (Spain); Stockholm Observatory (Sweden); Imperial College London, RAL, UCL-MSSL, UKATC, Univ. Sussex (UK); and Caltech, JPL, NHSC, Univ. Colorado (USA). This development has been supported by national funding agencies: CSA (Canada); NAOC (China); CEA, CNES, CNRS (France); ASI (Italy); MCINN (Spain); SNSB (Sweden); STFC, UKSA (UK); and NASA (USA).

References

- Abdo, A. A., Ackermann, M., Ajello, M., et al. 2009, *ApJ*, **703**, 1249
 Abdo, A. A., Ackermann, M., Ajello, M., et al. 2010, *A&A*, **512**, A7
 Anderl, S., Guillet, V., Pineau des Forêts, G., & Flower, D. R. 2013, *A&A*, **556**, A69
 Anderl, S., Gusdorf, A., & Güsten, R. 2014, *A&A*, **569**, A81
 André, P. 2011, in *Encyclopedia of Astrobiology*, eds. M. Gargaud, R. Amils, J. C. Quintanilla, H. J. J. Cleaves II, W. M. Irvine, D. L. Pinti, & M. Viso (Berlin Heidelberg: Springer), 1549
 Bakes, E. L. O., & Tielens, A. G. G. M. 1994, *ApJ*, **427**, 822
 Bekki, K., & Chiba, M. 2007, *PASA*, **24**, 21
 Besla, G., Kallivayalil, N., Hernquist, L., et al. 2012, *MNRAS*, **421**, 2109
 Bolatto, A. D., Israel, F. P., & Martin, C. L. 2005, *ApJ*, **633**, 210
 Book, L. G., Chu, Y.-H., & Gruendl, R. A. 2008, *ApJS*, **175**, 165
 Bron, E., Le Bourlot, J., & Le Petit, F. 2014, *A&A*, **569**, A100
 Carilli, C. L., & Walter, F. 2013, *ARA&A*, **51**, 105
 Carlson, L. R., Sewilo, M., Meixner, M., Romita, K. A., & Lawton, B. 2012, *A&A*, **542**, A66
 Chen, C.-H. R., Indebetouw, R., Chu, Y.-H., et al. 2010, *ApJ*, **721**, 1206
 Chu, Y.-H., Kennicutt, R. C., Snowdon, S. L., et al. 1997, *PASP*, **109**, 554
 Cooke, R., Kuncic, Z., Sharp, R., & Bland-Hawthorn, J. 2007, *ApJ*, **667**, L163
 Cormier, D., Madden, S. C., Lebouteiller, V., et al. 2015, *A&A*, **578**, A53
 Dawson, J. R., McClure-Griffiths, N. M., Wong, T., et al. 2013, *ApJ*, **763**, 56
 de Boer, K. S., Braun, J. M., Vallenari, A., & Mebold, U. 1998, *A&A*, **329**, L49
 de Graauw, T., Helmich, F. P., Phillips, T. G., et al. 2010, *A&A*, **518**, L6
 Dobbs, C. L., Krumholz, M. R., Ballesteros-Paredes, J., et al. 2014, *Protostars and Planets VI*, 3
 D’Onghia, E., & Fox, A. J. 2016, *ARA&A*, **54**, 363
 Draine, B. T. 1978, *ApJS*, **36**, 595
 Draine, B. T., & Li, A. 2007, *ApJ*, **657**, 810
 Fariña, C., Bosch, G. L., Morrell, N. I., Barbá, R. H., & Walborn, N. R. 2009, *AJ*, **138**, 510
 Flower, D. R., & Pineau des Forêts, G. 2003, *MNRAS*, **343**, 390
 Flower, D. R., & Pineau des Forêts, G. 2015, *A&A*, **578**, A63
 Fukui, Y., Mizuno, N., Yamaguchi, R., et al. 1999, *PASJ*, **51**, 745
 Fukui, Y., Harada, R., Tokuda, K., et al. 2015, *ApJ*, **807**, L4
 Fulton, T. R., Baluteau, J.-P., Bendo, G., et al. 2010, in *SPIE Conf. Ser.*, **7731**, 34
 Galametz, M., Hony, S., Galliano, F., et al. 2013, *MNRAS*, **431**, 1596
 Galliano, F., Hony, S., Bernard, J.-P., et al. 2011, *A&A*, **536**, A88

- Goldreich, P., & Kwan, J. 1974, *ApJ*, **189**, 441
- Goldsmith, P. F. 2001, *ApJ*, **557**, 736
- Gordon, K. D., Engelbracht, C. W., Rieke, G. H., et al. 2008, *ApJ*, **682**, 336
- Grenier, I. A., Black, J. H., & Strong, A. W. 2015, *ARA&A*, **53**, 199
- Greve, T. R., Leonidaki, I., Xilouris, E. M., et al. 2014, *ApJ*, **794**, 142
- Griffin, M. J., Abergel, A., Abreu, A., et al. 2010, *A&A*, **518**, L3
- Guillet, V., Pineau Des Forêts, G., & Jones, A. P. 2011, *A&A*, **527**, A123
- Gusdorf, A., Anderl, S., Güsten, R., et al. 2012, *A&A*, **542**, L19
- Gusdorf, A., Riquelme, D., Anderl, S., et al. 2015, *A&A*, **575**, A98
- Habart, E., Dartois, E., Abergel, A., et al. 2010, *A&A*, **518**, L116
- Hailley-Dunsheath, S., Sturm, E., Fischer, J., et al. 2012, *ApJ*, **755**, 57
- Hartigan, P., Raymond, J., & Hartmann, L. 1987, *ApJ*, **316**, 323
- Hartmann, D. H. 1999, *Proc. Nat. Acad. Sci.*, **96**, 4752
- Henize, K. G. 1956, *ApJS*, **2**, 315
- Herrera, C. N., Boulanger, F., Nesvadba, N. P. H., & Falgarone, E. 2012, *A&A*, **538**, L9
- Hollenbach, D. J., & Tielens, A. G. G. M. 1997, *ARA&A*, **35**, 179
- Indriolo, N., & McCall, B. J. 2012, *ApJ*, **745**, 91
- Israel, F. P., Güsten, R., Meijerink, R., et al. 2014, *A&A*, **562**, A96
- Jansen, D. J., van Dishoeck, E. F., & Black, J. H. 1994, *A&A*, **282**, 605
- Johansson, L. E. B., Olofsson, H., Hjalmarsen, A., Gredel, R., & Black, J. H. 1994, *A&A*, **291**, 89
- Jones, T. J., Woodward, C. E., Boyer, M. L., Gehrz, R. D., & Polomski, E. 2005, *ApJ*, **620**, 731
- Kamenetzky, J., Glenn, J., Rangwala, N., et al. 2012, *ApJ*, **753**, 70
- Kamenetzky, J., Rangwala, N., Glenn, J., Maloney, P. R., & Conley, A. 2014, *ApJ*, **795**, 174
- Kaufman, M. J., & Neufeld, D. A. 1996, *ApJ*, **456**, 611
- Kennicutt, R. C., & Evans, N. J. 2012, *ARA&A*, **50**, 531
- Kim, S., Staveley-Smith, L., Dopita, M. A., et al. 1998, *ApJ*, **503**, 674
- Kim, S., Dopita, M. A., Staveley-Smith, L., & Bessell, M. S. 1999, *AJ*, **118**, 2797
- Köhler, M., Habart, E., Arab, H., et al. 2014, *A&A*, **569**, A109
- Larson, R. L., Evans, II, N. J., Green, J. D., & Yang, Y.-L. 2015, *ApJ*, **806**, 70
- Launay, J. M., & Roueff, E. 1977, *A&A*, **56**, 289
- Le Bourlot, J., Pineau des Forêts, G., & Flower, D. R. 1999, *MNRAS*, **305**, 802
- Le Bourlot, J., Pineau des Forêts, G., Flower, D. R., & Cabrit, S. 2002, *MNRAS*, **332**, 985
- Le Bourlot, J., Le Petit, F., Pinto, C., Roueff, E., & Roy, F. 2012, *A&A*, **541**, A76
- Le Petit, F., Nehmé, C., Le Bourlot, J., & Roueff, E. 2006, *ApJS*, **164**, 506
- Lebouteiller, V., Cormier, D., Madden, S. C., et al. 2012, *A&A*, **548**, A91
- Lesaffre, P., Pineau des Forêts, G., Godard, B., et al. 2013, *A&A*, **550**, A106
- Lopez, L. A., Krumholz, M. R., Bolatto, A. D., et al. 2014, *ApJ*, **795**, 121
- Lu, N., Zhao, Y., Xu, C. K., et al. 2014, *ApJ*, **787**, L23
- Makiwa, G., Naylor, D. A., Ferlet, M., et al. 2013, *Appl. Opt.*, **52**, 3864
- Mashian, N., Sturm, E., Sternberg, A., et al. 2015, *ApJ*, **802**, 81
- Mathis, J. S., Mezger, P. G., & Panagia, N. 1983, *A&A*, **128**, 212
- Meijerink, R., & Spaans, M. 2005, *A&A*, **436**, 397
- Meijerink, R., Spaans, M., & Israel, F. P. 2007, *A&A*, **461**, 793
- Meijerink, R., Kristensen, L. E., Weiß, A., et al. 2013, *ApJ*, **762**, L16
- Meixner, M., Gordon, K. D., Indebetouw, R., et al. 2006, *AJ*, **132**, 2268
- Minamidani, T., Mizuno, N., Mizuno, Y., et al. 2008, *ApJS*, **175**, 485
- Mizuno, N., Yamaguchi, R., Mizuno, A., et al. 2001, *PASJ*, **53**, 971
- Mizuno, Y., Kawamura, A., Onishi, T., et al. 2010, *PASJ*, **62**, 51
- Neufeld, D. A., Lepp, S., & Melnick, G. J. 1995, *ApJS*, **100**, 132
- Nikolić, S., Garay, G., Rubio, M., & Johansson, L. E. B. 2007, *A&A*, **471**, 561
- Okada, Y., Requena-Torres, M. A., Güsten, R., et al. 2015, *A&A*, **580**, A54
- Ott, S. 2010, in *Astronomical Data Analysis Software and Systems XIX*, eds. Y. Mizumoto, K.-I. Morita, & M. Ohishi, *ASP Conf. Ser.*, **434**, 139
- Pagel, B. E. J. 2003, in *CNO in the Universe*, eds. C. Charbonnel, D. Schaerer, & G. Meynet, *ASP Conf. Ser.*, **304**, 187
- Papadopoulos, P. P., Zhang, Z.-Y., Xilouris, E. M., et al. 2014, *ApJ*, **788**, 153
- Pellegrini, E. W., Smith, J. D., Wolfire, M. G., et al. 2013, *ApJ*, **779**, L19
- Pietrzyński, G., Graczyk, D., Gieren, W., et al. 2013, *Nature*, **495**, 76
- Pilbratt, G. L., Riedinger, J. R., Passvogel, T., et al. 2010, *A&A*, **518**, L1
- Pineda, J. L., Mizuno, N., Stutzki, J., et al. 2008, *A&A*, **482**, 197
- Poglitsch, A., Waelkens, C., Geis, N., et al. 2010, *A&A*, **518**, L2
- Pon, A., Johnstone, D., Kaufman, M. J., Caselli, P., & Plume, R. 2014, *MNRAS*, **445**, 1508
- Press, W. H., Teukolsky, S. A., Vetterling, W. T., & Flannery, B. P. 1992, *Numerical recipes in FORTRAN, The art of scientific computing* (Cambridge University Press)
- Putman, M. E., Staveley-Smith, L., Freeman, K. C., Gibson, B. K., & Barnes, D. G. 2003, *ApJ*, **586**, 170
- Rangwala, N., Maloney, P. R., Glenn, J., et al. 2011, *ApJ*, **743**, 94
- Rangwala, N., Maloney, P. R., Wilson, C. D., et al. 2015, *ApJ*, **806**, 17
- Rigopoulou, D., Hurley, P. D., Swinyard, B. M., et al. 2013, *MNRAS*, **434**, 2051
- Rosenberg, M. J. F., Kazandjian, M. V., van der Werf, P. P., et al. 2014a, *A&A*, **564**, A126
- Rosenberg, M. J. F., Meijerink, R., Israel, F. P., et al. 2014b, *A&A*, **568**, A90
- Rosenberg, M. J. F., van der Werf, P. P., Aalto, S., et al. 2015, *ApJ*, **801**, 72
- Schirm, M. R. P., Wilson, C. D., Parkin, T. J., et al. 2014, *ApJ*, **781**, 101
- Schlegel, E. M., Marshall, F. E., Mushotzky, R. F., et al. 1994, *ApJ*, **422**, 243
- Seale, J. P., Looney, L. W., Wong, T., et al. 2012, *ApJ*, **751**, 42
- Spinoglio, L., Pereira-Santaella, M., Busquet, G., et al. 2012, *ApJ*, **758**, 108
- Stock, D. J., Wolfire, M. G., Peeters, E., et al. 2015, *A&A*, **579**, A67
- Stutzki, J., & Winnewisser, G. 1985, *A&A*, **144**, 13
- Swinyard, B. M., Ade, P., Baluteau, J.-P., et al. 2010, *A&A*, **518**, L4
- Tielens, A. G. G. M. 2005, *The Physics and Chemistry of the Interstellar Medium* (Cambridge University Press)
- Tielens, A. G. G. M., & Hollenbach, D. 1985, *ApJ*, **291**, 722
- van der Marel, R. P., & Cioni, M.-R. L. 2001, *AJ*, **122**, 1807
- van der Tak, F. F. S., Black, J. H., Schöier, F. L., Jansen, D. J., & van Dishoeck, E. F. 2007, *A&A*, **468**, 627
- van der Werf, P. P., Isaak, K. G., Meijerink, R., et al. 2010, *A&A*, **518**, L42
- Walker, K. M., Song, L., Yang, B. H., et al. 2015, *ApJ*, **811**, 27
- Weingartner, J. C., & Draine, B. T. 2001, *ApJS*, **134**, 263
- Weingartner, J. C., Draine, B. T., & Barr, D. K. 2006, *ApJ*, **645**, 1188
- Williams, R. M., Petre, R., Chu, Y.-H., & Chen, C.-H. R. 2000, *ApJ*, **536**, L27
- Williams, B. J., Borkowski, K. J., Reynolds, S. P., et al. 2006, *ApJ*, **652**, L33
- Wolfire, M. G., Hollenbach, D., McKee, C. F., Tielens, A. G. G. M., & Bakes, E. L. O. 1995, *ApJ*, **443**, 152
- Wolszczan, A., Cordes, J. M., & Dewey, R. J. 1991, *ApJ*, **372**, L99
- Wong, T., Hughes, A., Ott, J., et al. 2011, *ApJS*, **197**, 16
- Wu, B., Van Loo, S., Tan, J. C., & Bruderer, S. 2015a, *ApJ*, **811**, 56
- Wu, R., Madden, S. C., Galliano, F., et al. 2015b, *A&A*, **575**, A88
- Wu, B., Tan, J. C., Nakamura, F., et al. 2016, *ApJ*, submitted
ArXiv e-prints [[arXiv:1606.01320](https://arxiv.org/abs/1606.01320)]
- Yang, B., Stancil, P. C., Balakrishnan, N., & Forrey, R. C. 2010, *ApJ*, **718**, 1062

Appendix A: FTS CO, [CI], [NII] integrated intensity images

We present the FTS CO, [CI], and [NII] integrated intensity images of N159W (Sect. 2.1.2 for details on how we derive these images). All images have a resolution of $42''$ (~ 10 pc at the LMC distance) and a pixel size of $30''$. For CO(4–3) and CO(9–8), the first CO transitions in the SLW and SSW, the SLW and SSW arrays are shown as the blue and green crosses, except the central detectors for the first jiggle observation

(SLWC3 and SSWD4) in yellow and orange. The spectra with $S/N_s > 5$ (“detections”) are overlaid in red, while those with $S/N_s \leq 5$ (“non-detections”) are in blue. To show the x -axis (in GHz) and y -axis (in $10^{-18} \text{ W m}^{-2} \text{ Hz}^{-1} \text{ sr}^{-1}$ except for CO(13–12), which is in $10^{-19} \text{ W m}^{-2} \text{ Hz}^{-1} \text{ sr}^{-1}$) ranges, the spectrum of the pixel observed with SLWC3 and SSWD4 is presented in the bottom right corner of each figure. Finally, the $2'$ unvignetted field-of-view for FTS observations is indicated as the black dashed circle.

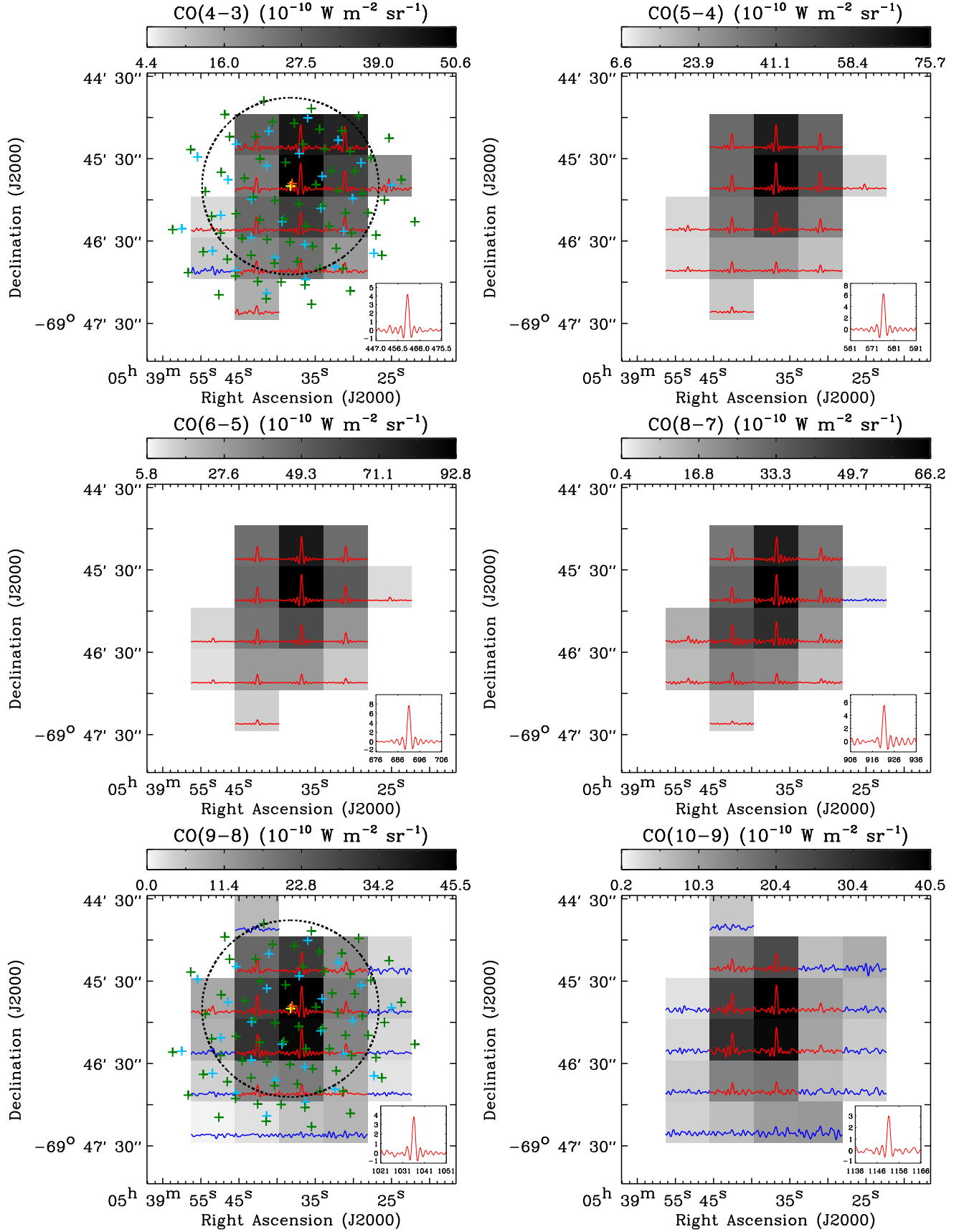


Fig. A.1. FTS CO, [CI], and [NII] integrated intensity images of N159W. See Appendix A for details in the figures.

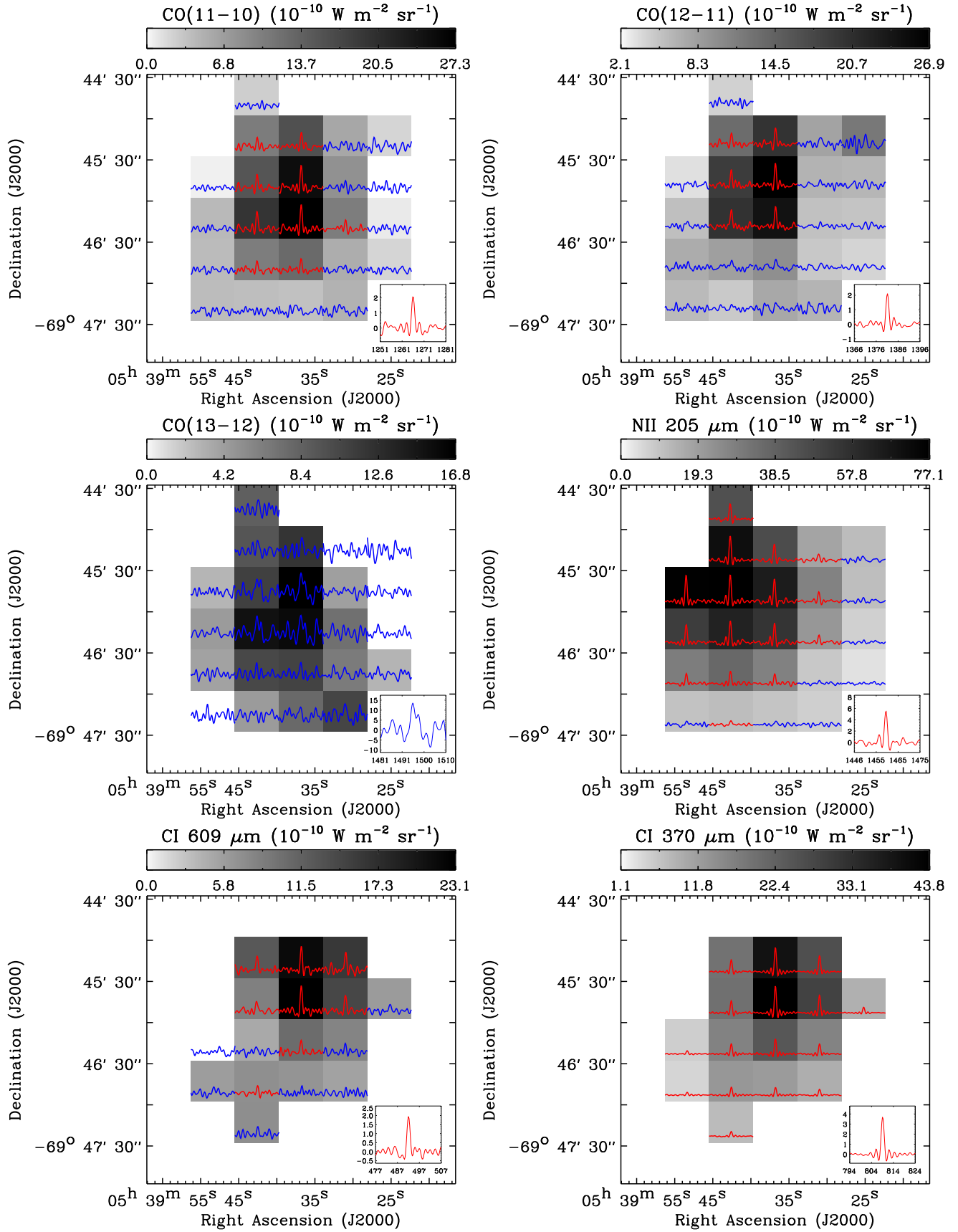


Fig. A.1. continued.

Appendix B: Paris-Durham shock models with half solar metallicity

We present some of the results from the shock models with $0.5 Z_{\odot}$. To simulate the propagation of shocks in the half solar metallicity ISM, we run the Paris-Durham code as we do for $1 Z_{\odot}$, but with metal (C, N, O, Mg, Si, S, and Fe), grain, and PAH abundances reduced by half. The geometrical properties of grains and PAHs remain the same. For our test runs, the shock parameters that reproduce the CO observations of N159W are used (Sect. 5.3.2): $n_{\text{pre}} = 10^4 \text{ cm}^{-3}$, $b = 1$, $G'_{\text{UV}} = 0$, and $v_s = 6$,

10, and 14 km s^{-1} . Note that this is the first attempt to run the Paris-Durham code with $Z < 1 Z_{\odot}$.

We find that the difference between the two models in terms of the CO (up to $J = 13$ – 12) and fine-structure line ([CII] $158 \mu\text{m}$, [OI] $63 \mu\text{m}$, and [OI] $145 \mu\text{m}$) intensities is less than a factor of two (e.g., Fig. B.1). This small difference arises from the fact that shocks have similar thermal structures in the $1 Z_{\odot}$ and $0.5 Z_{\odot}$ models. As a result, the difference in the line intensities primarily comes from the difference in atomic/molecular abundances (e.g., less than a factor of two for CO at CO-bright shocked layers).

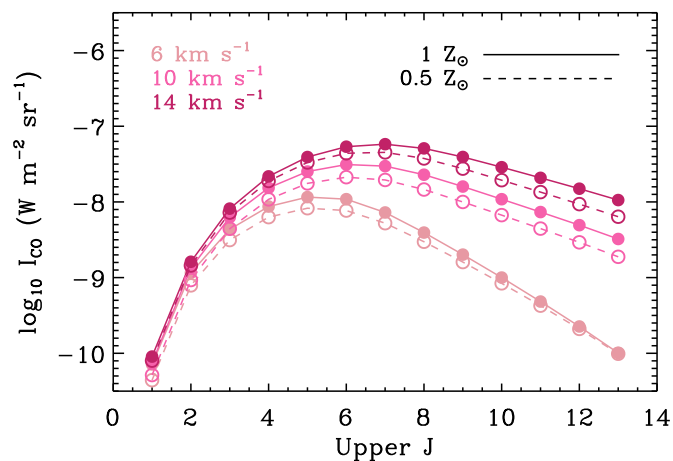


Fig. B.1. Comparison between the shock models with $1 Z_{\odot}$ (solid line) and $0.5 Z_{\odot}$ (dashed line). For the comparison, the shock parameters that reproduce the CO observations of N159W are used (Sect. 5.3.2): $n_{\text{pre}} = 10^4 \text{ cm}^{-3}$, $b = 1$, $G'_{\text{UV}} = 0$, and $v_s = 6$, 10, and 14 km s^{-1} . Note that the data points in this plot are direct model predictions (no beam filling factor applied).